

# Design of small hand-launched solar-powered UAVs: From concept study to a multi-day world endurance record flight

---

Philipp Oettershagen, Amir Melzer, Thomas Mantel, Konrad Rudin, Thomas Stastny, Bartosz Wawrzacz, Timo Hinzmann, Stefan Leutenegger\*, Kostas Alexis<sup>†</sup> and Roland Siegwart

Autonomous Systems Lab  
Swiss Federal Institute of Technology Zurich (ETH Zurich)  
Leonhardstrasse 21  
8092 Zurich  
+41 44 632 7395  
philipp.oettershagen@mavt.ethz.ch

## Abstract

We present the development process behind *AtlantikSolar*, a small 6.9 kg hand-launchable low-altitude solar-powered Unmanned Aerial Vehicle (UAV) that recently completed an 81-hour continuous flight and thereby established a new flight endurance world record for all aircraft below 50 kg mass. The goal of our work is to increase the usability of such solar-powered robotic aircraft by maximizing their *perpetual flight robustness* to meteorological deteriorations such as clouds or winds. We present energetic system models and a design methodology, implement them in our publicly-available conceptual design framework for perpetual flight-capable solar-powered UAVs, and finally apply the framework to the *AtlantikSolar* UAV. We present the detailed *AtlantikSolar* characteristics as a practical design example. Airframe, avionics, hardware, state estimation and control method development for autonomous flight operations are described. Flight data is used to validate the conceptual design framework. Flight results from the continuous 81-hour and 2338 km covered ground distance flight show that *AtlantikSolar* achieves 39% minimum state-of-charge, 6.8 h excess time and 6.2 h charge margin. These performance metrics are a significant improvement over previous solar-powered UAVs. A performance outlook shows that *AtlantikSolar* allows perpetual flight in a 6-month window around June 21<sup>st</sup> at mid-European latitudes, and that multi-day flights with small optical- or infrared-camera payloads are possible for the first time. The demonstrated performance represents the current state-of-the-art in solar-powered low-altitude perpetual flight performance. We conclude with lessons learned from the three-year *AtlantikSolar* UAV development process and with a sensitivity analysis that identifies the most promising technological areas for future solar-powered UAV performance improvements.

---

\*now Lecturer, Imperial College London ; Work performed while at ETH Zurich.

<sup>†</sup>now Assistant Professor, University of Nevada, Reno ; Work performed while at ETH Zurich.

# 1 Introduction

## 1.1 Solar-powered Unmanned Aerial Vehicles

Solar-electrically powered fixed-wing Unmanned Aerial Vehicles (UAVs) promise significantly increased flight endurance over purely-electrically or even gas-powered aerial vehicles. A solar-powered UAV uses excess solar energy gathered during the day to recharge its batteries. Typical UAV applications such as industrial and agricultural sensing and mapping clearly benefit from this increased flight endurance. Given an appropriate design and suitable environmental conditions, the stored energy may even be enough to continuously keep the UAV airborne during the night and, potentially, subsequent day-night cycles. This so called *perpetual flight* capability makes solar-powered UAVs great candidates for applications in which data needs to be collected or distributed either continuously or on a large scale. Large-scale disaster relief support missions, meteorological surveys in remote areas and continuous border or maritime patrol would benefit in particular from this multi-day continuous flight capability (Colella & Wenneker, 1996).

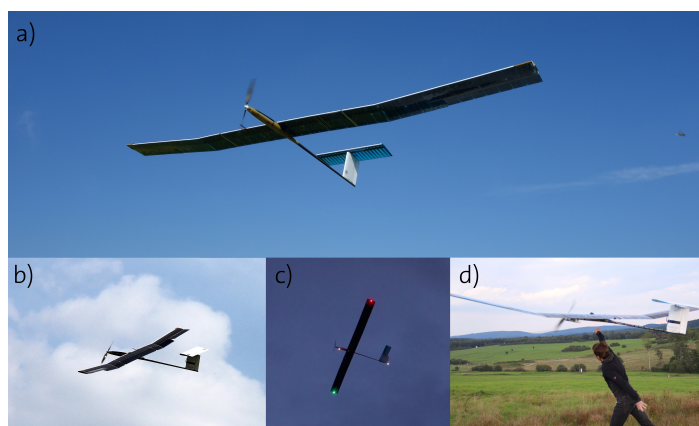


Figure 1: The *AtlantikSolar* solar-powered low-altitude long-endurance (LALE) UAV: a) After take-off b) exposing the solar cells and engaged spoilers c) after a night flight d) during hand-launch in a Search-and-Rescue research mission with the sensing and processing pod attached below the left wing. Images a) and c) are from the continuous 28-hour *perpetual endurance* demonstration flight on June 30<sup>th</sup> 2015.

Solar-powered flight is not a new concept, but dates back to the 1970s. A comprehensive historical overview is provided by Boucher (1984) and Noth (2008b). One important facet of solar-powered flight is solar-powered High-Altitude Long-Endurance (HALE) operation. The ground work in this area was laid by NASA's ERAST programme (Colella & Wenneker, 1996). Recently, interest in employing similar large-scale (wingspan above 20 m) solar-powered HALE UAVs as *atmospheric satellites* - i.e. stationary/loitering platforms e.g. for telecommunications relay - has peaked. Notable examples of this trend are *Solara* (Ackerman, 2013) and *Zephyr*, which has already demonstrated a continuous flight of 14 days (QinetiQ, 2010) and is the first solar-powered HALE UAV to enter commercial operations (Osborne, 2016).

In contrast, smaller scale solar-powered UAVs are mostly designed for Low-Altitude Long-Endurance (LALE) applications. Though faced with the more challenging meteorological phenomena of the lower atmosphere (clouds, rain, wind gusts and thermals), low-altitude UAVs provide the advantages of higher resolution imaging with reduced cloud obstruction, lower complexity and cost and simplified handling e.g. through hand-launchability. As a result, solar-powered LALE UAVs aiming to reach flight times up to 14 hours have been studied in academia (Weider et al., 2007; Malaver, Gonzalez, Motta, & Villa, 2015) and industry (AeroVironment, 2013; ByeAerospace, 2015). However, research targeting perpetual endurance in these small-scale robotic aircraft has been relatively sparse. Most research focusses on conceptual design studies without extensive flight experience, e.g. (Morton, Scharber, & Papanikolopoulos, 2013; Morton, D'Sa, & Papanikolopoulos, 2015). Projects that have demonstrated *perpetual flight* are *SoLong* (Cocconi, 2005), which performed a continuous 48-hour flight using solar power while actively seeking out thermal updrafts,

and SkySailor (Noth, 2008a), which demonstrated a 27-hour solar-powered continuous flight without the use of thermals. However, these UAVs were mainly developed to demonstrate the *feasibility of perpetual flight* for the first time, and do neither provide sufficient robustness against deteriorated meteorological conditions (e.g. clouds or downwinds) nor the capability to fly perpetually with common sensing payloads. For example, the SkySailor UAV crossed the night with only 5.8% of remaining battery energy.

## 1.2 Contributions of this Paper

Succeeding the work by Cocconi (2005) and Noth (2008a), this paper represents the *next evolutionary step* in the development of solar-powered LALE UAVs by not only focusing on the already challenging task of demonstrating the *feasibility* of perpetual flight, but — for the first time — on achieving *energetic robustness* in perpetual flight. We present the complete development process behind our 6.9 kg *AtlantikSolar* UAV (Figure 1) and present extensive flight results from its recent continuous and solely solar-powered flight of 81 hours (4 days and 3 nights) and 2338 km ground distance — the flight which holds the current flight endurance *world record* for all aircraft below 50 kg mass. This paper consequently aims to establish the state-of-the-art in solar-powered perpetual flight of low-altitude robotic aircraft by introducing and extending relevant aspects from the two central disciplines — solar-powered aircraft design and aerial robotics — that together have enabled this achievement. The specific contributions of this paper are:

- Section 2 presents energetic system models as well as a derived conceptual design and analysis software framework and contributes a novel formal methodology that allows to design solar-powered UAVs for energetically-robust *perpetual flight* in sub-optimal meteorological conditions.
- Section 3 presents the detailed design of the *AtlantikSolar* (AS-2) UAV. The focus lies on combining efficient aircraft systems with a simple yet robust and efficient infrastructure for robotic flight. This paper introduces the chosen avionics hardware and contributes on-board state estimation and control algorithms that have been tailored specifically towards solar-powered UAVs.
- Section 4 presents and analyzes the continuous solar-powered 81-hour flight by *AtlantikSolar* AS-2. The results validate the design approach and indicate significantly improved energetic margins (*perpetual flight* with up to 39% remaining battery energy). This flight of *AtlantikSolar* also represents the current world record in flight endurance for all aircraft below 50 kg mass.
- Section 5 contributes an outlook into the exact conditions (day-of-year, latitude, meteorological conditions) and sensing payloads with which today’s technology allows specific solar-powered *perpetual flight* missions. A sensitivity analysis answers which technology improvements promise the largest future improvements in solar-powered UAV performance.

This paper extends our previous work, which presented the initial system design and flight results of the first prototype *AtlantikSolar* UAV (Oettershagen, Melzer, Mantel, Rudin, Lotz, et al., 2015), introduced aerial sensing and mapping applications (Oettershagen, Stastny, et al., 2015), and demonstrated *AtlantikSolar*’s first *perpetual flight* (Oettershagen et al., 2016) of 28-hour duration. Sections 2 and 3 have been significantly extended with respect to this prior work, and sections 4 and 5 are completely new contributions. In conjunction with this paper, we release both the conceptual design and analysis software framework at (Oettershagen, 2016b) and the 81-hour continuous flight dataset at (Oettershagen, 2016a).

## 2 Conceptual Design

The conceptual design phase represents a multi-dimensional optimization of aircraft design variables that aims to improve the aircraft performance metrics under certain user-specified environmental conditions and user-imposed design constraints. As described before, the central design paradigm in this paper is that we aim to increase aircraft performance in the sense that the solar-powered perpetual flight *robustness* with respect to changed operating conditions (latitude or time) or deteriorated local meteorological conditions

(e.g. clouds or wind) is maximized. The vehicle realized towards that goal, the *AtlantikSolar* UAV, is designed using the methodology shown in Figure 2. This Matlab-based conceptual design and analysis framework (CDAF) for solar-powered UAVs was developed at ETH Zurich and is based on (Noth, 2008a; Leutenegger, Jabas, & Siegwart, 2010). In conjunction with this paper, its source-code has been released at (Oettershagen, 2016b). This paper and our CDAF use the following terminology:

- *Design variables* are varied to optimize the aircraft performance. For solar-powered UAVs, we chose the wing span  $b$ , aspect ratio  $\lambda$  and battery mass  $m_{\text{bat}}$  as design variables.
- *Performance metrics* represent the aircraft performance, and shall thus be optimized. We choose the excess time  $T_{\text{exc}}$  and the charge margin  $T_{\text{cm}}$  as the central performance metrics.
- *Technological parameters* are material- or technology-properties (e.g. solar module efficiency) that are assumed to be given, i.e. they are generally fixed.
- *User inputs* are requirements on the aircraft design specified by the user. This can be technical (payload mass or size) or operational (altitude, latitude, time) requirements.

The CDAF architecture and its main modules, the *Core Module* and *Performance Evaluation Module*, are shown in Figure 2. In the following, section 2.1 presents the equations behind the aircraft sizing and performance simulation. Section 2.2 introduces the performance metrics and contributes extensions to existing optimization methodologies that allow to maximize *perpetual flight* robustness, section 2.3 applies that extended methodology to the conceptual design of the *AtlantikSolar* UAV, and finally section 2.4 investigates the expected vehicle performance in deteriorated operating conditions.

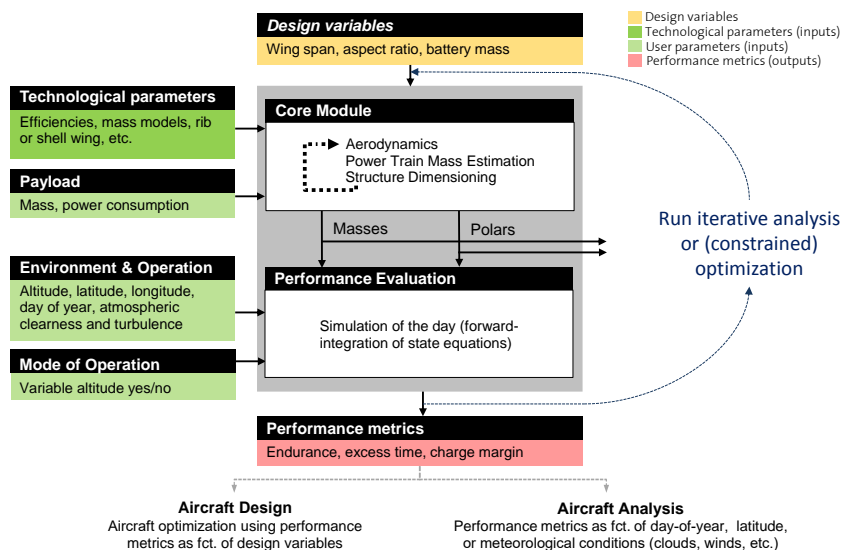


Figure 2: The solar-powered UAV conceptual design and analysis framework (CDAF). The framework can be used either for aircraft *design* using a simple graphical performance optimization or for aircraft *analysis* e.g. in the form of a robustness analysis against different operating- or meteorological-conditions.

## 2.1 System Models for Solar-Powered UAVs

The simple quasi-static energy input/output-models for solar-powered UAVs used for example by Noth (2008a) and Leutenegger et al. (2010) typically neglect the UAV’s kinetic energy and only model the electric energy  $E_{\text{bat}}$  in the aircraft batteries and the altitude  $h$  as a representation of the potential energy  $E_{\text{pot}}$ . The two resulting state equations are forward-integrated to assess the energy flows and the energetic safety margins that a solar-powered UAV provides with respect to *perpetual flight*. A typical simulation result is

shown in Figure 3. The combined state equation may be written as

$$\frac{dE_{\text{bat}}}{dt} = \mu_{\text{bat}} \cdot P_{\text{bat}} \approx \mu_{\text{bat}} \cdot (P_{\text{solar}} - P_{\text{out}}) \quad (1)$$

$$\frac{dh}{dt} = \frac{1}{m_{\text{tot}} \cdot g} \cdot (\eta_{\text{prop}} \cdot P_{\text{prop}} - P_{\text{level}}) \quad (2)$$

In Eq. (1)  $\mu_{\text{bat}}$  considers charge- and discharge-losses and thus  $\mu_{\text{bat}} = \mu_{\text{bat}}^{\text{chg}} \leq 1$  for  $P_{\text{bat}} > 0$  and  $\mu_{\text{bat}} = \mu_{\text{bat}}^{\text{dchg}} \geq 1$  for  $P_{\text{bat}} < 0$ . In Eq. (2) we have  $dh/dt = 0$  for the special case of level flight. The equation does not yet consider the fact that for  $P_{\text{solar}} > P_{\text{out}}$  the charge-power going into the batteries needs to be limited. Using the maximum relative charge factor  $f_{\text{mrc}}$ , we define the absolute maximum charge power  $P_{\text{bat}}^{\text{chg,max}} = f_{\text{mrc}} \cdot E_{\text{bat}}^{\text{max}}$  as a percentage of the maximum battery capacity. Knowing that  $P_{\text{bat}}^{\text{chg}} > 0$ , we now propose

$$P_{\text{bat}}^{\text{chg}} = \begin{cases} 0 & \text{if } \sigma_{\text{bat}} \geq 1 \\ \exp(-c_1 \cdot \frac{\sigma_{\text{bat}} - \sigma_{\text{bat}}^{\text{cl}}}{1 - \sigma_{\text{bat}}^{\text{cl}}}) \cdot P_{\text{bat}}^{\text{chg,max}} & \text{if } \sigma_{\text{bat}} > \sigma_{\text{bat}}^{\text{cl}} \\ \min(P_{\text{solar}} - P_{\text{out}}, P_{\text{bat}}^{\text{chg,max}}) & \text{otherwise} \end{cases} \quad (3)$$

Equations (1–3) form an extended energy state equation that implements exponentially-decreasing charge power limiting (Figure 3) as generally suggested for the Lithium-based batteries (Panasonic, 2014) that are in use on the majority of solar-powered UAVs today. The battery state-of-charge (SoC) is  $\sigma_{\text{bat}} = E_{\text{bat}}/E_{\text{bat}}^{\text{max}}$ , the SoC (or  $E_{\text{bat}}$ ) where the exponentially decreasing charge limiting begins is  $\sigma_{\text{bat}}^{\text{cl}}$  (or  $E_{\text{bat}}^{\text{cl}}$ ), and  $c_1$  is a constant that is determined from the desired final charge power  $\lim_{\sigma_{\text{bat}} \rightarrow 1} P_{\text{bat}}^{\text{chg}} = P_{\text{bat}}^{\text{chg,final}} = f_{\text{frc}} \cdot E_{\text{bat}}^{\text{max}}$  using  $c_1 = -\ln(f_{\text{frc}})$ . The total required electric output power in Eqs. (1) and (3) is

$$P_{\text{out}} = P_{\text{prop}} + P_{\text{av}} + P_{\text{pld}}. \quad (4)$$

$P_{\text{av}}$  and  $P_{\text{pld}}$  are user inputs and represent the required avionics- and payload power. The main contribution comes from the required electric propulsion power  $P_{\text{prop}}$ . In the important case of level-flight,  $P_{\text{prop}} = P_{\text{level}}/\eta_{\text{prop}}$ , where  $\eta_{\text{prop}}$  includes the propeller, gearbox, motor, and motor-controller efficiencies. To derive the required level flight power  $P_{\text{level}}$ , we use the static equilibrium of lift force  $F_{\text{L}}$  and drag force  $F_{\text{D}}$

$$F_{\text{L}} = 1/2 \cdot \rho \cdot C_{\text{L}} \cdot A_{\text{wing}} \cdot v_{\text{air}}^2 = m_{\text{tot}} \cdot g \quad (5)$$

$$F_{\text{D}} = 1/2 \cdot \rho \cdot C_{\text{D}} \cdot A_{\text{wing}} \cdot v_{\text{air}}^2. \quad (6)$$

Here,  $g$  is the local earth gravity,  $\rho$  is the local and thus altitude-dependent air density,  $A_{\text{wing}}$  is the wing area and  $m_{\text{tot}}$  is the total airplane mass. Combining and inserting Eqs. (5),(6) into  $P_{\text{level}} = F_{\text{D}} \cdot v_{\text{air}}$  and minimizing with respect to the airspeed  $v_{\text{air}}$  yields the minimum required aerodynamic level-flight power

$$P_{\text{level}} = \left( \frac{C_{\text{D}}(v_{\text{air}})}{C_{\text{L}}^{\frac{3}{2}}(v_{\text{air}})} \right)_{\min} \sqrt{\frac{2(m_{\text{tot}}g)^3}{\rho \cdot A_{\text{wing}}}}. \quad (7)$$

The airplane lift and drag coefficients  $C_{\text{L}}$  and  $C_{\text{D}}$  are both a function of airspeed. They consist of, first, the wing profile lift and drag coefficients  $C_{\text{L,wing}}$  and  $C_{\text{D,wing}}$  that are retrieved as a function of the Reynolds-Number  $Re$  from 2-D airfoil simulations using XFOil (Drela, 2001). In a second and third step, the airplane fuselage and stabilizer parasitic drag  $C_{\text{D,par}}$  and induced drag  $C_{\text{D,ind}}$  are added through

$$C_{\text{D,par}} = 0.074 \cdot Re^{-0.2} \quad (8)$$

$$C_{\text{D,ind}} = \frac{C_{\text{L}}^2}{\pi \cdot e_0 \cdot \lambda}. \quad (9)$$

The former equation represents a simplification assuming flat-plate friction. In the latter,  $e_0 \approx 0.92$  is the Oswald efficiency and  $\lambda$  the wing aspect ratio. The total airplane mass in Eq. (7) is represented by

$$m_{\text{tot}} = m_{\text{bat}} + m_{\text{struct}} + m_{\text{prop}} + m_{\text{sm}} + m_{\text{mppt}} + m_{\text{av}} + m_{\text{pld}}. \quad (10)$$

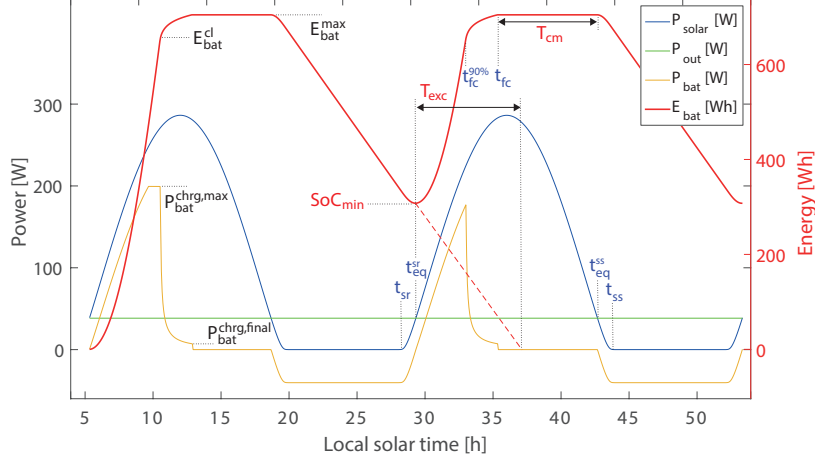


Figure 3: Energetic simulation of the *AtlantikSolar* UAV configuration with  $b = 5.6$  m,  $\lambda = 18.5$  and  $m_{\text{bat}} = 2.9$  kg showing input power, output power and battery energy over a 2-day flight. The *performance metrics* (red) are the excess time  $T_{\text{exc}}$ , charge margin  $T_{\text{cm}}$  and the minimum state-of-charge  $\sigma_{\text{bat}}^{\text{min}}$ . The *characteristic times* (blue) are the sunrise and sunset times  $t_{\text{sr}}$  and  $t_{\text{ss}}$ , the power equality times where  $P_{\text{solar}} = P_{\text{out}}$  after sunrise  $t_{\text{eq}}^{\text{sr}}$  and before sunset  $t_{\text{eq}}^{\text{ss}}$ , and the times when the charge process has reached  $\sigma_{\text{bat}} = 90\%$  and  $\sigma_{\text{bat}} = 100\%$  are  $t_{\text{fc}}^{90\%}$  and  $t_{\text{fc}}$ . Parameters governing the battery charge process are printed in black. In the simulation, the charge rate limiting is active, but altitude changes are not allowed.

In our approach, the battery mass  $m_{\text{bat}}$  is considered a design (i.e. to be optimized) variable and  $m_{\text{av}}$  and  $m_{\text{pld}}$  are user inputs based on pre-determined requirements. All other variables are automatically sized by our conceptual design environment: The structure mass  $m_{\text{struct}}$  is automatically calculated as a function of the aircraft geometry, the total mass and pre-specified maximum load cases according to (Leutenegger et al., 2010). Automatic sizing is applied to the propulsion system mass  $m_{\text{prop}} = k_{\text{prop}} \cdot P_{\text{prop}}^{\text{max}}$ , the solar module mass  $m_{\text{sm}} = k_{\text{sm}} \cdot A_{\text{sm}}$  and the maximum power point tracker (MPPT) mass  $m_{\text{mppt}} = k_{\text{mppt}} \cdot P_{\text{solar}}^{\text{max}}$ . Here,  $P_{\text{prop}}^{\text{max}}$  is a function of the maximum climb rate desired by the user,  $P_{\text{solar}}^{\text{max}}$  is the maximum expected solar power income,  $A_{\text{sm}} = f_{\text{sm}} \cdot A_{\text{wing}}$  is the exposed solar module area with relative fill-factor  $f_{\text{sm}}$  and the other variables are constants defined in Table 1. The power income through solar radiation is modeled as

$$P_{\text{solar}}^{\text{nom}} = I_{\text{solar}}(\varphi_{\text{lat}}, h, \delta, t, \vec{n}_{\text{sm}}) \cdot A_{\text{sm}} \cdot \eta_{\text{sm}} \cdot \eta_{\text{mppt}}. \quad (11)$$

Here,  $I_{\text{solar}}(\varphi_{\text{lat}}, h, \delta, t, \vec{n}_{\text{sm}})$  is the solar radiation on a unit ( $1\text{m}^2$ ) area and is modeled after (Duffie & Beckman, 2006). It is a function of geographical latitude  $\varphi_{\text{lat}}$ , altitude  $h$ , current day-of-year  $\delta$ , local time  $t$  and solar module normal vector  $\vec{n}_{\text{sm}}$ . For the conceptual design, the solar module area  $A_{\text{sm}} = \text{const}$  is considered a horizontally-oriented area given that the exact orientation of course depends on the specific mission profile (see section 3.3.1). Thus, assuming an inertial aircraft-centered North-East-Down (NED) frame of reference, we choose  $\vec{n}_{\text{sm}} = [0, 0, -1]$ . The solar module efficiency  $\eta_{\text{sm}} = \eta_{\text{sm}}^{\text{STC}} \cdot \epsilon_{\text{sm}}^{\text{cbr}}$  includes an efficiency reduction factor due to the wing camber, and the maximum power point tracker efficiency is  $\eta_{\text{mppt}}$ .

## 2.2 Extension of the Conceptual Design Methodology

In this paper, we build upon the conceptual design tool described at the beginning of this section but extend it as follows: First, we now provide the capability to perform energetic simulations of multi-day solar-powered flight, whereas before only one day-night cycle was considered. Figure 3 shows the results for incoming solar power  $P_{\text{solar}}$ , required power  $P_{\text{out}}$ , and remaining battery charge  $E_{\text{bat}}$  obtained for a flight of two subsequent day-night cycles. Clearly, the initial charge condition  $E_{\text{bat}}$  at time of sunrise  $t_{\text{sr}} = \min(t(P_{\text{solar}} > 0))$  for the second day is different than on the first day and thus significantly influences the re-charging process.

Second, and more importantly, the optimization criteria are extended to achieve energetically robust multi-

Table 1: Technological parameters used during the conceptual design process of *AtlantikSolar*. While all parameters were at first estimated or based on previous projects (Noth, 2008a), the parameter set presented and used in this paper is already augmented with measurements on initial small-scale component prototypes.

Name	Value	Description	Source
$\eta_{sm}^{STC}$	0.237	Solar module efficiency at Standard Test Conditions (STC)	Measured
$\epsilon_{sm}^{cbr}$	0.97	Solar module efficiency factor due to wing camber	(Noth, 2008a)
$\eta_{mppt}$	0.95	MPPT efficiency	(Noth, 2008a)
$\eta_{prop}$	0.62	Combined propeller, gearbox, motor & controller efficiency	(Noth, 2008a)
$\mu_{bat}^{chrg}$	0.95	Battery charge efficiency coefficient	(Noth, 2008a)
$\mu_{bat}^{dchrg}$	1.03	Battery discharge efficiency coefficient	(Noth, 2008a)
$e_{bat}$	251 Wh/kg	Battery specific energy (includes cabling and insulation)	Measured
$f_{sm}$	0.85	Solar module fill factor	Estimated
$k_{sm}$	590 g/m <sup>2</sup>	Solar module areal density	Measured
$k_{mppt}$	0.422 g/W	MPPT mass constant	(Noth, 2008a)
$k_{prop}$	1.1 g/W	Propulsion system mass constant	(Noth, 2008a)
$m_{av}$	1.22 kg	Avionics mass (includes all cabling and fittings)	User input
$m_{pld}$	0.0 kg	Payload mass	User input
$P_{av}$	6 W	Avionics power consumption	User input
$P_{pld}$	0.0 W	Payload power consumption	User input
$f_{mrc}$	0.5	Maximum relative charge power factor	Design choice
$f_{fc}$	0.04	Final relative charge power factor	Design choice
$\sigma_{bat}^{cl}$	0.9	State-of-charge to begin exponential charge limiting	Design choice

day flight. A necessary and sufficient condition for *perpetual flight* is that the excess time  $T_{exc} > 0$ , where

$$T_{exc} = \frac{E_{bat}(t = t_{eq})}{P_{out}^{nom}} \Big|_{P_{solar}(t > t_{sr})=0} \quad (12)$$

with power-equality time  $t_{eq} = t(P_{solar}^{nom} = P_{out}^{nom})$  in the morning. This means that remaining battery capacity has to exist at  $t = t_{eq}$  to continue flight for instance in case of cloud coverage. An alternative performance metric stating the same fact is the minimum battery state-of-charge

$$\sigma_{bat}^{min} = \min \left( \frac{E_{bat}(t)}{E_{bat}^{max}} \right) \quad (13)$$

where we require that  $\sigma_{bat}^{min} > 0$  throughout the whole flight but specifically at  $t = t_{eq}$  in the morning. Previous literature and the authors in (Noth, 2008a; Leutenegger et al., 2010) focus on maximizing  $T_{exc}$  (or, equivalently,  $\sigma_{bat}^{min}$ ). However, a large  $T_{exc}$  does not provide direct robustness against decreases in  $P_{solar}$  e.g. due to cloud cover during the charging process. In contrast, when optimizing purely for  $T_{exc}$ , the methodology presented here would select the largest battery size (due to the scaling of  $P_{level}$  with  $m_{bat}$ ) which can be fully charged under optimal conditions, but every reduction in  $P_{solar}$  will directly decrease  $T_{exc}$  due to only partially charged batteries. Thus, we introduce the charge margin

$$T_{cm} = T(E_{bat} = E_{bat}^{max}) := t_{eq}^{ss} - t_{fc} \quad (14)$$

as a safety margin that indicates how much unused charging time remains after reaching full charge before the battery discharge begins again. This also means that in case of decreased solar power income,  $T_{cm} > 0$  provides additional margin before a decrease in excess time occurs. We calculate  $T_{cm}$  from the difference between the equality time before sunset and the full charge time.

In this paper, the overall approach for increasing robustness with respect to local power disturbances is thus to determine the lowest acceptable  $T_{exc}$  satisfying the user's requirements on the UAV operation, and then

to optimize the configuration for  $T_{\text{cm}}$ . The exact procedure proposed for the design of solar-powered UAVs for robust *perpetual flight* is:

- Step 1** Selection of nominal operating latitude  $\varphi_{\text{lat}}$ , day-of-year  $\delta^{\text{nom}}$  and the outermost days where perpetual UAV endurance is required  $\delta^{\text{min,max}}$
- Step 2** Retrieval of the night durations  $T_{\text{night}}^{\text{min}}$ ,  $T_{\text{night}}^{\text{max}}$  from (Duffie & Beckman, 2006) for the range  $\delta = [\delta^{\text{min}}, \delta^{\text{max}}]$
- Step 3** The total required excess time is now

$$T_{\text{exc}}^{\text{req}} = T_{\text{exc}}^{\delta} + T_{\text{exc}}^{\text{clouds}} + T_{\text{exc}}^{P_{\text{level}}}, \quad (15)$$

where  $T_{\text{exc}}^{\delta} = T_{\text{night}}^{\text{max}} - T_{\text{night}}^{\text{min}}$  is a margin for the changing night duration,  $T_{\text{exc}}^{\text{clouds}}$  is a margin for clouds in the morning or evening, and  $T_{\text{exc}}^{P_{\text{level}}}$  represents a margin for increased power consumption e.g. due to downdrafts or uncertainties in  $P_{\text{out}}$ .

- Step 4** Design analysis given the methodology in section 2.3 for  $\delta(T_{\text{night}} = T_{\text{night}}^{\text{min}})$ . Pre-selection of the subset  $\mathcal{S}$  of configurations satisfying  $T_{\text{exc}} > T_{\text{exc}}^{\text{req}}$
- Step 5** Allowance for a set of intermediate configurations  $\mathcal{S}_i$  within  $\mathcal{S}$  while taking UAV-specific constraints on  $b$ ,  $\lambda$ , or  $m_{\text{bat}}$  into account. Selection of the final configuration  $\mathcal{S}_f$  from  $\mathcal{S}_i$  in order to obtain the largest charge margin  $T_{\text{cm}}$ .

This conceptual design methodology is applied in section 2.3 below. An alternative conceptual design approach proposed by Morton et al. (2013) utilizes a weighted - but to some extent arbitrary - combination of  $T_{\text{exc}}$  and  $T_{\text{cm}}$ . The advantage of our methodology is that it explicitly guarantees the feasibility of *perpetual flight* over a range of operating dates and environmental conditions by enforcing the energetic margins  $T_{\text{exc}}^{\delta}$ ,  $T_{\text{exc}}^{\text{clouds}}$  and  $T_{\text{exc}}^{P_{\text{level}}}$  which are directly derived from user- and thus mission requirements.

## 2.3 Application of the Conceptual Design Methodology

For *Step 1* of the conceptual design methodology of section 2.2, we define that the *AtlantikSolar* UAV shall operate at a nominal latitude of  $\varphi_{\text{lat}} = 47^\circ\text{N}$  and shall provide perpetual endurance within a  $\pm 2$  month window centered around  $\delta^{\text{nom}} = \text{June } 21^{\text{st}}$  (April  $21^{\text{st}}$ –August  $21^{\text{st}}$ ). Using (Duffie & Beckman, 2006) for *Step 2*, we find  $T_{\text{night}}^{\text{min}} = 8.7$  h (June  $21^{\text{st}}$ ),  $T_{\text{night}}^{\text{max}} = 10.5$  h (April  $21^{\text{st}}$ ), and thus  $T_{\text{exc}}^{\delta} = 1.8$  h. In *Step 3* we employ previous flight experience to choose  $T_{\text{exc}}^{\text{clouds}} = 3.0$  h to account for three hours of full cloud coverage either on the evening or the morning and choose  $T_{\text{exc}}^{P_{\text{level}}} = 0.2 \cdot T_{\text{night}}^{\text{max}} = 2.1$  h to cover increased power consumption due to modeling errors, downdrafts or headwinds. Using Eq. (15), we retrieve  $T_{\text{exc}}^{\text{req}} = 6.9$  h as the minimum required excess time for robust *perpetual flight* at the given dates and locations.

In *Step 4*, the conceptual design software framework of Figure 2 is now applied over the design variables wing span  $b$ , battery mass  $m_{\text{bat}}$  and aspect ratio  $\lambda$ . The technological parameters and user inputs are taken from Table 1. The initial analysis of a range of aspect ratios  $\lambda$  indicates that optimum performance occurs around  $\lambda = 18.5$ , for which Figure 4 shows the resulting performance margins versus the design variables  $b$  and  $m_{\text{bat}}$ . The excess time (top left) allows to quickly identify the regions in which *perpetual flight* is possible. For the cases in which *perpetual flight* is impossible, the endurance plot (top right) shows that the total achievable flight times are still significant and often above 30 hours. The flight endurance  $T_{\text{endur}}$  is herein calculated assuming launch with full batteries and landing when  $E_{\text{bat}} = 0$ . The charge margin (lower left) shows the expected increase for smaller battery mass, and the total airplane mass (lower right) scales with battery mass and wing span as described in section 2.1. The final element of *Step 4* is to identify the subset  $\mathcal{S}$  of configurations satisfying  $T_{\text{exc}} > T_{\text{exc}}^{\text{req}}$ . In Figure 4, this is the region within the blue contour-line. In general, the optimum performance metrics occur at large wing spans.

We begin *Step 5* by enforcing the user- and design-specific UAV constraints. The first is that for our aerial vehicle, we aim for a small-scale and hand-launchable configuration that allows easy transportation

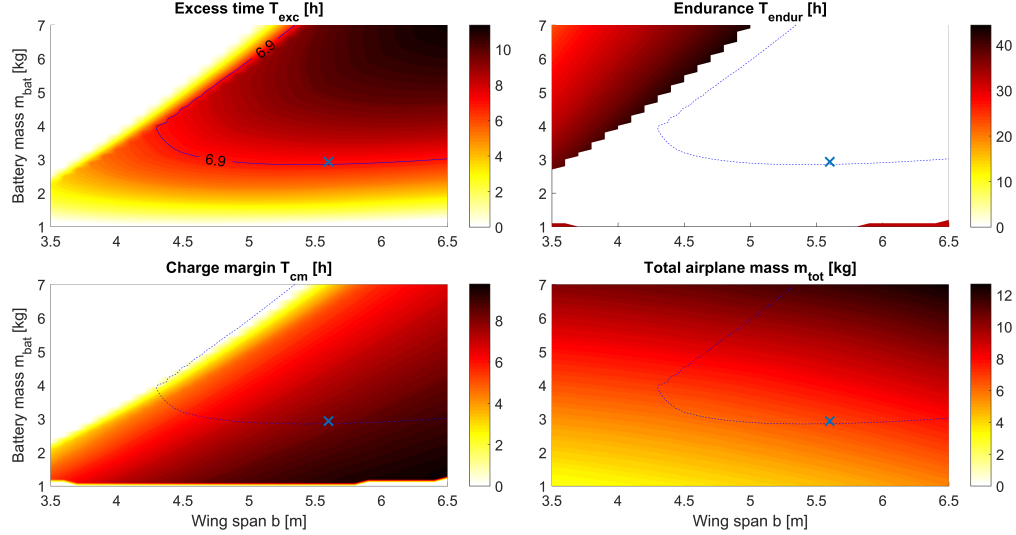


Figure 4: Conceptual design performance results for *AtlantikSolar* as a function of  $b$  and  $m_{\text{bat}}$  (calculation step size 0.1 m and 0.1 kg respectively), all at  $\lambda = 18.5$ . White points in the plots indicate N/A or zero values. The configuration subset  $\mathcal{S}$  satisfying  $T_{\text{exc}} > T_{\text{exc}}^{\text{req}}$  under our design requirements lies inside the blue contour line. The chosen final configuration  $\mathcal{S}_f = (\mathcal{S}|_{m_{\text{bat}}=2.9 \text{ kg}, b=5.6 \text{ m}, \lambda=18.5})$  is marked with a blue cross.

via disassembly of the main wing. Thus we enforce the design constraint that each of our three main wing sections shall have less than 2 m span and therefore choose  $b = 5.6$  m. A second significant design constraint affecting small-scale solar-powered UAVs is the need to seamlessly integrate the solar cells (in this case 125mm-wide solar cells, see section 3.1) inside both the wing chord and the wing span. The final choice of  $b = 5.6$  m and  $\lambda = 18.5$  shown in Figure 4 fulfills this design constraint and provides near-optimal performance over the range of available aspect ratios. The last design choice is  $m_{\text{bat}}$ , for which we seek to optimize  $T_{\text{cm}}$  within the previously selected set  $\mathcal{S}_i = (\mathcal{S}|_{b=5.6 \text{ m}, \lambda=18.5})$ . As visible in Figure 4,  $m_{\text{bat}} = [2.8 \text{ kg}, 7.0 \text{ kg}]$  lies within  $\mathcal{S}_i$ . We choose  $m_{\text{bat}} = 2.9$  kg to optimize  $T_{\text{cm}}$  and due to practical battery sizing constraints described in section 3.1. The selected final configuration  $\mathcal{S}_f = (\mathcal{S}|_{m_{\text{bat}}=2.9 \text{ kg}, b=5.6 \text{ m}, \lambda=18.5})$  yields an estimated  $T_{\text{exc}} = 7.03$  h and  $T_{\text{cm}} = 8.17$  h at  $m_{\text{tot}} = 7.12$  kg and an expected required total system power  $P_{\text{out}} = 41.8$  W for the nominal operating date, latitude and altitude.

## 2.4 Initial Robustness Analysis

To perform an initial verification of the multi-day flight robustness provided by the conceptual design and analysis framework in the form of the *AtlantikSolar* UAV, we investigate its performance under deviations from its nominal operating point. The most significant deviations are caused by local and often unpredictable meteorological effects that alter the UAV’s energy balance. These deteriorations can be modeled by a change in the average UAV power income and output over the day, namely

- (a) The disturbed solar power income  $P_{\text{solar}}^{\text{dist}}$ , as caused by clouds or fog. We define  $k_{\text{CCF}} \in [0, 1]$  as a factor governing the cloud cover and thus the clearness of the atmosphere. Lacking knowledge of the exact spatial and temporal disturbance distribution, we assume  $P_{\text{solar}}^{\text{dist}}(t) = P_{\text{solar}}^{\text{nom}}(t) \cdot k_{\text{CCF}}$ .
- (b) The disturbed electric power output  $P_{\text{out}}^{\text{dist}}$ . Wind downdrafts, head wind, or gusts may require increased propulsion or actuation power. By introducing  $k_{\text{OPF}}$  as the Output Power Factor, we can define  $P_{\text{out}}^{\text{dist}}(t) = P_{\text{out}}^{\text{nom}}(t) \cdot k_{\text{OPF}}$

Figure 5 shows the excess time  $T_{\text{exc}}$  as a function of these disturbances. The *AtlantikSolar* UAV configuration developed using our novel design approach ( $m_{\text{bat}} = 2.9$  kg) still provides perpetual endurance with less than 50% of the solar power income or if more than 50% increased power are required on June 21<sup>st</sup> (Figure

5a). On April 21<sup>st</sup>, *AtlantikSolar* still provides solid robustness (Figure 5b), which verifies the  $\delta^{\text{nom}} \pm 2$  month perpetual endurance requirement. In contrast, a configuration optimized to give maximum excess time ( $m_{\text{bat}} = 6.2$  kg, Figure 5c) via previous conceptual design approaches (Noth, 2008a; Leutenegger et al., 2010) yields a higher maximum  $T_{\text{exc}}$  of 10.1 h, but the robustness with respect to clouds or higher required level power is greatly decreased. On April 21<sup>st</sup>, the  $m_{\text{bat}} = 6.2$  kg configuration (Figure 5d) cannot provide reliable perpetual endurance anymore. Overall, through the extended optimization criteria of section 2.2, our design approach results in significantly higher energetic robustness - and thus increased operational flexibility and safety in multi-day flights - when compared to configurations that are purely optimized for maximum excess time. Note that section 5 provides a more detailed robustness analysis and performance outlook including operation at different latitudes and days of the year for the final *AtlantikSolar* UAV.

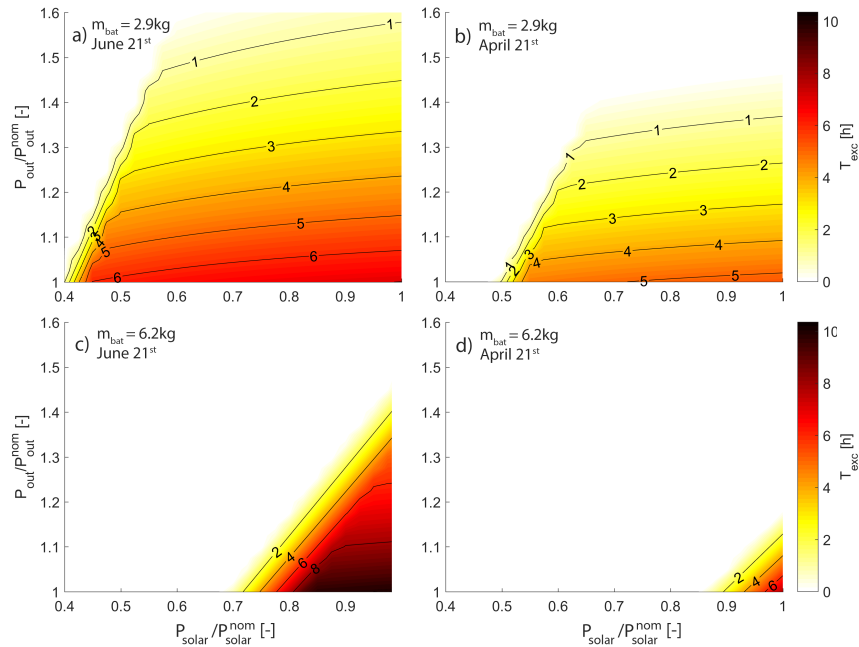


Figure 5:  $T_{\text{exc}}$  under disturbed power input and -output for the  $b = 5.6$  m,  $\lambda = 18.5$  configuration: a)  $m_{\text{bat}} = 2.9$  kg on June 21<sup>st</sup> b)  $m_{\text{bat}} = 2.9$  kg on April 21<sup>st</sup> c)  $m_{\text{bat}} = 6.2$  kg on June 21<sup>st</sup> d)  $m_{\text{bat}} = 6.2$  kg on April 21<sup>st</sup>

### 3 Detailed Design

Three design characteristics are decisive for the application of *perpetual flight*-capable robotic aircraft in common sensing- and mapping missions. First, an efficient UAV platform (section 3.1) that maximizes the *perpetual flight* robustness while still providing good handling- and deployment-qualities (e.g. hand-launch through a single person) is required. Second, as human intervention shall be minimal, robust and reliable autopilot hardware and -software are required. Section 3.1 covers the developed sensor- and autopilot-infrastructure, and section 3.2 contributes the simple yet robust and effective estimation and flight control approaches that are optimized for the challenging flight dynamics of solar-powered UAVs. Third, the UAV needs to provide interfaces for modern miniaturized optical- and infrared imaging payloads. The *AtlantikSolar* UAV combines all three aspects and thereby enables autonomous long-endurance aerial sensing and -mapping applications as shown in (Oettershagen, Stastny, et al., 2015).

### 3.1 UAV Platform Design

#### 3.1.1 Airframe

The *AtlantikSolar* UAV airframe (Figure 6) is of a conventional glider-like T-tail configuration with two ailerons, an all-moving elevator and a rudder. The 5.69 m wide wing consists of three pieces of similar span that can be disassembled before transport. The wings are perfectly rectangular, i.e. neither swept nor tapered, to house the two rows of solar cells over the whole wing span. They use a custom-designed MH139-F wing profile of 11.6% relative thickness, possess 3° of wing twist to avoid stall at the wing tips and thus at the ailerons, and incorporate a dihedral angle of 7° on the outer wings to increase the aircraft's eigenstability around the roll axis. The airframe characteristics are summarized in Table 2.

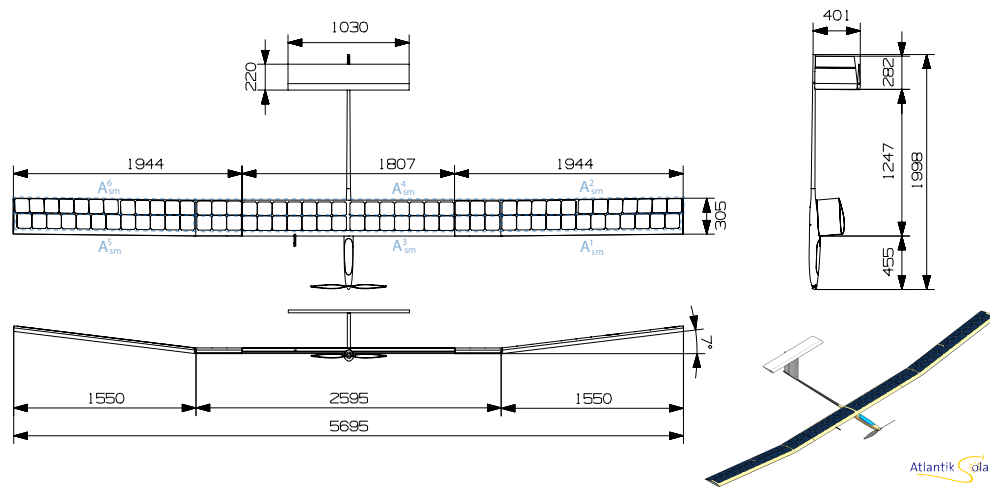


Figure 6: The *AtlantikSolar* UAV airframe. Dimensions are given in mm. The solar module geometry of the surfaces  $A_{sm}^i$  is given in light blue.

The wing and stabilizers of *AtlantikSolar* are built in a traditional rib-spar construction method (Figure 7). The whole structure is designed to withstand maximum vertical loads of up to  $n_z^{\max} = 4g$ , upon which - as usual for the design of carbon-fiber based structural elements - a safety factor of 1.8 for a total of 7.2g's is added. The wing's main element is a cylindrical carbon-fiber spar that takes the torsional loads and restricts the wing torsion to less than 1.5° per semi-wing-span under the maximum vertical load  $n_z^{\max}$  to avoid solar cell damage. Four carbon-fiber belts of trapezoidal and laterally-varying cross-section are attached above and below the spar to optimally resist bending loads and to provide wing stiffness. The single fuselage is constructed from aramid- and glass-fiber reinforced plastics and connects to the rear T-tail via a carbon fiber spar. The all-moving elevator and the rudder use a Drela HT14 profile with an increased relative thickness of 9.5%. The HT14 profile is specifically designed for tail surfaces, exhibits very low pressure drag, and its increased thickness provides the cross-sectional area to reach the required structural stiffness at low mass.

#### 3.1.2 Energy Generation and Storage

The energy generation and storage system is at the core of *AtlantikSolar*'s multi-day flight capability. The whole system is connected to one central power bus (Figure 8) that runs through the aircraft central wing. Energy storage is handled by 60 cylindrical high energy density Lithium-Ion batteries (Panasonic NCR18650b, new cells measured to provide 251 Wh/kg energetic density) that are fitted into the cylindrical wing spars to optimally distribute the mass in a *span loader* concept. The cells are connected in a 6S (21.6 V) configuration and provide  $E_{bat}^{\max} = 733$  Wh at  $m_{bat} = 2.92$  kg. Energy is generated through solar modules that incorporate 88 SunPower E60 cells. They provide a measured module-level efficiency of  $\eta_{sm}^{STC} = 23.7\%$ , an areal density of  $k_{sm} = 590$  g/m<sup>2</sup> and a maximum power output of 275 W at  $\varphi_{lat} = 47^\circ N$  on June 21<sup>st</sup>. The solar modules

Table 2: *AtlantikSolar* design characteristics. See Figure 6 for further details.

Parameter	Value
Wing span	5.69 m
Wing chord	0.305 m
Total mass*	6.93 kg
Battery mass	2.92 kg
Max. payload mass	0.9 kg
Flight speed*	8.6 m/s (cruise), 7.4 m/s (stall)

\*With batteries, no payload

are seamlessly embedded in the upper wing surface to avoid premature flow separation. To increase operational performance and safety, the complete energy generation and storage system is operated and monitored via custom-made Maximum Power Point Trackers (MPPTs) and a battery management system. These are responsible for regulating the energy flow, providing detailed energy flow information (including  $P_{\text{solar}}$ ,  $P_{\text{out}}$  and  $P_{\text{bat}}$  used in the later sections), and for monitoring the overall and cell-level charge states.

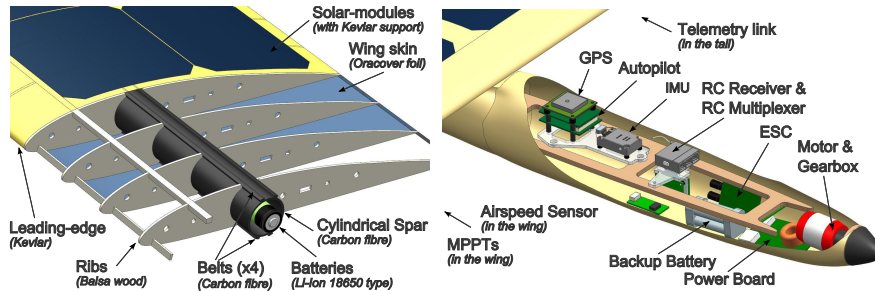


Figure 7: Left: Wing structure with integrated batteries and solar cells. Right: Fuselage arrangement with the main avionics compartment. The foldable propeller is omitted for clarity.

### 3.1.3 Propulsion and Actuation

The actuation system consists of four Volz DA 15-N servos that drive the two ailerons, the all-moving elevator and the rudder. The brushless servos provide contactless position feedback, IP67 splash water protection, EMI shielding, and a motor overload protection system. In order to assess the reliability of the actuation system over a multi-day flight, the Volz actuators were successfully operated in a servo test-bed for 30 days under flight-equivalent loads (DellaCa, 2013). The propulsion system is driven by a RS-E Strecker 260.20 brushless DC motor with  $k_V = 470 \text{ RPM/V}$  and a Kontronik Koby 55 LV motor controller. An all-steel planetary gearbox with four pinion gears and a 5:1 reduction ratio and a foldable custom built carbon-fiber propeller with diameter  $D = 0.66 \text{ m}$  and pitch  $H = 0.6 \text{ m}$  are attached to the motor output shaft. The gearbox was selected for its good reliability characteristics after other smaller-sized gearboxes showed in-air failures during long-endurance flights (see section 6). The maximum electric input power the propulsion system can handle is around  $P_{\text{prop}}^{\text{burst}} = 420 \text{ W}$  for up to 20 s and up to  $P_{\text{prop}}^{\text{max}} = 220 \text{ W}$  continuously.

### 3.1.4 Avionics

To allow reliable long-endurance robotic flight, the avionics subsystem (Figures 7 and 8) is designed for simplicity, robustness and low power consumption. It is centered around a Pixhawk PX4 Autopilot (Meier, Honegger, & Pollefeys, 2015) — an open-source software and open-source hardware project initiated at ETH Zurich — which provides a real-time operating system and features a 168 MHz Cortex M4F microprocessor

with 192 KB RAM. For attitude estimation (section 3.2.1), an ADIS16448 10-Degrees of Freedom (DOF) Inertial Measurement Unit (IMU), a u-blox LEA-6H GPS receiver, and a Sensirion SDP600 differential pressure sensor have been interfaced to the autopilot. The airspeed sensing system exhibits less than 5% total error at  $v_{\text{air}} \approx 8 \text{ m/s}$ , which is essential to closely track the low power-optimal airspeed  $v_{\text{air}}^{\text{opt}}$  (see section 3.3.3). Both a 433 MHz medium-range telemetry link and a long-range Iridium-based satellite backup link are integrated. The airplane implements a fully manual RC-command fall-back mode to deal with a severe case of autopilot failure. Night operations are possible due to four on-board high-power indicator LEDs.

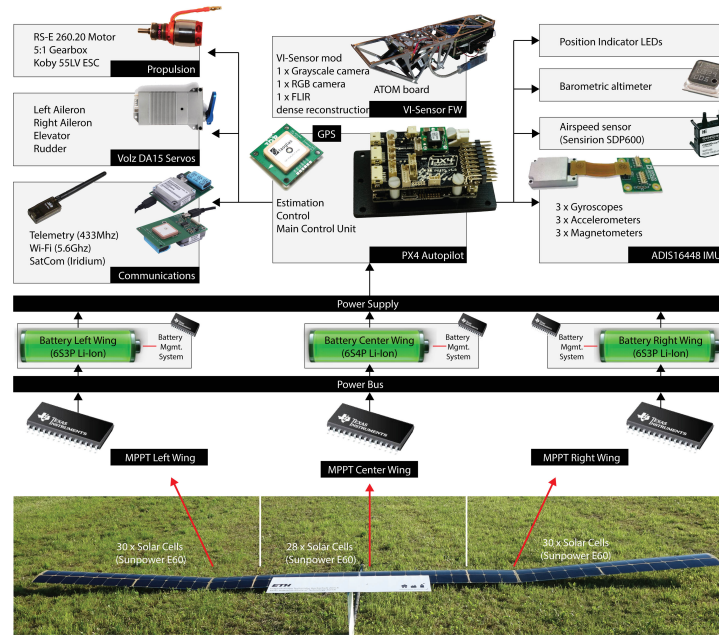


Figure 8: Topological system overview over the *AtlantikSolar* UAV.

### 3.1.5 Payload

The *AtlantikSolar* UAV has been flown with payloads up to  $m_{\text{pld}} = 900 \text{ g}$ . More specifically, the sensor and processing unit in Figure 9 ( $m_{\text{pld}} = 480 \text{ g}$  including cameras, mounted beneath the wing) has been designed at ETH Zurich to allow environment perception and long-endurance aerial mapping. It incorporates a *visual-inertial sensor system* (Nikolic et al., 2014) and a small form factor computer based on a quad-core Intel Atom processor. The former consists of an ARM-FPGA system, an ADIS16448 IMU as well as two cameras - a FLIR Tau 2 for Long-Wavelength Infrared (LWIR) and an Aptina MT9V034 for visible light

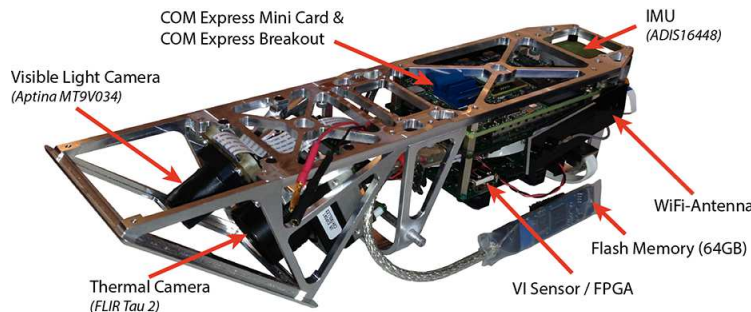


Figure 9: The sensing and processing unit that integrates optical imaging, thermal imaging and on-board processing. The unit can be mounted below the wing of the *AtlantikSolar* UAV.

imaging - and allows accurate real-time SLAM (Leutenegger, 2014). The latter runs Ubuntu and the Robot Operating System (ROS) and is intended for higher-level tasks such as path planning, high-level control and victim detection (Vempati, Agamennoni, Stastny, & Siegwart, 2015). Moreover, it is equipped with WiFi-communication to transmit a video feed to the ground. Further details on the sensor pod and its operation in multiple Search-and-Rescue research applications are given in (Oettershagen, Stastny, et al., 2015).

### 3.2 UAV State Estimation and Flight Control

*Perpetual endurance* autonomous flight requires a robotic system that is robust to failures of primary sensors, employs control methods that can handle the challenging flight dynamics of solar-powered UAVs, and includes decision logic to react to disturbances or uncommon events (e.g. a thermal updraft that carries the system beyond its altitude limits). The software methods that implement this behavior are described in the following.

#### 3.2.1 State Estimation

To provide reliable and drift-free long-term autonomous operation, a light-weight EKF-based state estimator (Leutenegger, Melzer, Alexis, & Siegwart, 2014) is implemented on the autopilot. It fuses data from the IMU with the magnetometer, GPS-Position, GPS-velocity and airspeed measurements to successively estimate position, velocity, orientation, mean sea level static pressure (QFF) as well as accelerometer and gyro biases. Robustness against temporal GPS failure is provided through the inclusion of airspeed measurements from a differential pressure sensor. To increase flight safety, the algorithm estimates the local three-dimensional wind vector and employs an internal aircraft aerodynamics model to estimate the current sideslip angle and Angle of Attack (AoA), which can then be used by the flight controller to apply implicit flight regime limits (Oettershagen, Melzer, Leutenegger, Alexis, & Siegwart, 2014).

#### 3.2.2 System Identification

Towards aiding the control synthesis procedure, a simplified linear state-space representation of the UAV dynamics was derived based on recorded flight data and frequency-domain system identification methods. For approximately level flight, linear models may capture the vehicle response for small perturbations around a given equilibrium. Decoupling the longitudinal and lateral axis, the dynamics of a UAV may take the form presented in (Dorobantu, Murch, Mettler, & Balas, 2011) and used in the authors' previous work (Oettershagen et al., 2014). Within this work, the exact aforementioned lateral dynamics representation is employed, while the longitudinal dynamics are extended to account for the effect of throttle and are expressed as

$$\begin{aligned} \mathbf{M}_{\text{lon}} \dot{\hat{\mathbf{x}}}_{\text{lon}} &= \mathbf{A}'_{\text{lon}} \hat{\mathbf{x}}_{\text{lon}} + \mathbf{B}'_{\text{lon}} \mathbf{u}_{\text{lon}} \\ \hat{\mathbf{x}}_{\text{lon}} &= \begin{bmatrix} \hat{u} & \hat{w} & \hat{q} & \hat{\theta} \end{bmatrix}^T \end{aligned} \quad (16)$$

where  $\hat{u}, \hat{w}, \hat{q}, \theta$  correspond to the predicted body  $x$ -,  $z$ -axis velocities, the pitch rate and the pitch angle, respectively.  $\mathbf{u}_{\text{lon}} = [u_{\text{elev}} \ u_{\text{throt}}]^T$  corresponds to the elevator deflection and the throttle command, respectively. In

$$\begin{aligned} \mathbf{M}_{\text{lon}} &= \begin{bmatrix} m_{\text{tot}} & 0 & 0 & 0 \\ 0 & m_{\text{tot}} & 0 & 0 \\ 0 & 0 & I_y & 0 \\ 0 & 0 & 0 & 1 \end{bmatrix}, \quad \mathbf{B}'_{\text{lon}} = \begin{bmatrix} X_{u_{\text{elev}}} & X_{u_{\text{throt}}} \\ Z_{u_{\text{elev}}} & Z_{u_{\text{throt}}} \\ M_{u_{\text{elev}}} & M_{u_{\text{throt}}} \\ 0 & 0 \end{bmatrix} \\ \mathbf{A}'_{\text{lon}} &= \begin{bmatrix} X_u & X_w & X_q - m_{\text{tot}} W_e & -m_{\text{tot}} g \cos \theta_e \\ Z_u & Z_w & Z_q + m_{\text{tot}} U_e & -m_{\text{tot}} g \sin \theta_e \\ M_u & M_w & M_q & 0 \\ 0 & 0 & 1 & 0 \end{bmatrix} \end{aligned} \quad (17)$$

Table 3: Estimated modes of the longitudinal and lateral system dynamics

Mode	Natural Frequency (rad/s)	Damping Ratio
<i>Longitudinal Dynamics</i>		
Phugoid	0.586	0.789
Short-Period Pole 1	7.8	-
Short-Period Pole 2	8.1	-
<i>Lateral Dynamics</i>		
Spiral	0.82	-
Dutch Roll	7.52	0.414
Roll	3.49	-

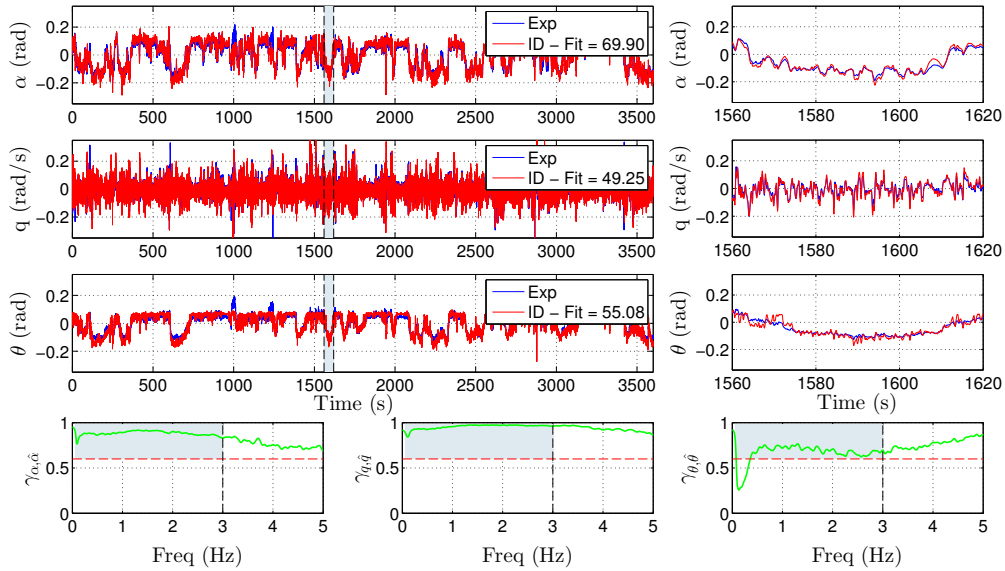


Figure 10: Longitudinal dynamics system identification validation. The AoA  $\alpha$  is computed based on the experimental and model-predicted values for  $u$  and  $w$ . Results for 1 h are shown along with a closer look to 60 s of the flight and the coherence values  $\gamma$  between the experimental  $\alpha, q, \theta$  and the predicted  $\hat{\alpha}, \hat{q}, \hat{\theta}$ .

$W_e, U_e, \theta_e$  are the trim points of  $u, w, \theta$  and the elements of  $\mathbf{M}'_{\text{lon}}, \mathbf{A}'_{\text{lon}}$  and  $\mathbf{B}'_{\text{lon}}$  form the stability and control derivatives of the longitudinal dynamics based on the identified terms and the inertia term  $I_y$ .

Towards high-fidelity system identification, a structured way of defining persistently exciting signals, evaluating the quality of the flight data, conducting frequency-domain identification and evaluating the derived model quality was employed. All four  $u_{\text{elev}}, u_{\text{throt}}, u_{\text{ail}}, u_{\text{rud}}$  inputs that excite the vehicle longitudinal and lateral dynamics are manipulated using chirp-like signals that cover a wide spectrum area expected to contain the dominant vehicle dynamics. For every recorded dataset, the quality of the signals was evaluated using the coherence metric between every input  $u_i$  and its correlated outputs  $y_j$ . The employed frequency-domain system identification framework is based on the objective function and guidelines outlined by Tischler and Remple (2012), who state that a coherence  $\gamma_{u_i, y_j} \geq 0.6$  indicates a good chance to identify a linear relationship between these two signals. Employing the same methods and their specific extensions in our previous work (Oettershagen et al., 2014), models of sufficient fidelity were derived for the *AtlantikSolar* UAV. The increased coherence values in Figure 10 indicate that the linearity assumption within the respective flight envelope subset is effectively correct. Similar results are also derived for the lateral dynamics. The identified linear aircraft model is then used for initial tuning of the linear inner-loop flight controller described in section 3.2.3. Note that the trim point was around level flight and specifically

$U_e = 9.8 \text{ m/s}$ ,  $W_e = 0.5 \text{ m/s}$ ,  $\theta_e = 0.056 \text{ rad}$ ,  $v_e = 0 \text{ m/s}$ ,  $p_e = q_e = r_e = 0$ . Table 3 presents the main frequency characteristics of the derived approximate system dynamics.

### 3.2.3 Flight Control and Guidance

The *AtlantikSolar* UAV features autonomous navigation up to the level of loitering and tracking of user-defined waypoints. The complete control structure (Figure 11) is tuned offline based on the system model identified in the previous section, then functionality-tested in an X-Plane 10 Hardware-In-the-Loop (HIL) simulation and finally refined in extensive flight tests. For inner-loop control, our baseline-solution corresponds to a set of cascaded and saturated PID controllers: The Stability Augmentation System (SAS) applies rate-damping to shape the airplane’s frequency response, while the Control Augmentation System (CAS) applies proportional-integral feedback to achieve roll ( $\phi$ ) and pitch ( $\theta$ ) reference tracking. All control actions are in their final stage adapted with respect to the dynamic pressure  $q = \frac{1}{2}\rho v_{\text{air}}^2$  which accounts for the change of the effective moments created by the control surfaces. Due to the specific design characteristics of solar-powered UAVs such as *AtlantikSolar* (high aspect ratio and thus high inertia especially in  $I_z$  and  $I_x$ , limited admissible structural loads) the following extensions for the inner-loop controllers were implemented:

- *Coordinated turn control*: Smooths the adverse yaw behavior and tracks the no-sideslip yaw (in body coordinates) rate  $r = \frac{g \cdot \sin(\phi)}{v_{\text{air}}}$ .
- *Overspeed protection*: Works through an integrator that slowly forces a pitch up. The protection’s output  $u_{\text{elev}}^{\text{Ovspd}}$  is only added to the final output  $u_{\text{elev}}$  if  $v_{\text{air}} > 1.2 \cdot v_{\text{air}}^{\text{max}}$  and  $\theta < 0$ , otherwise the integrator is zeroed to avoid pitch overshoots after a recovery from an overspeed condition.
- *Static output limiters*: Applied on all outputs to avoid overload of the structure.
- *Dynamic overload protection*: Constantly monitors the vertical aircraft acceleration and limits the elevator command dynamically to guarantee that  $n_z < n_z^{\text{lim}}$ . Given that  $n_z^{\text{max}} = 4g$  for *AtlantikSolar*, we choose  $n_z^{\text{lim}} = 2.5g$ . Note that the dynamic overload protection is not applied to  $u_{\text{elev}}^{\text{Ovspd}}$  to not overrule the overspeed protection. The structural integrity is nevertheless guaranteed because the integrator behind  $u_{\text{elev}}^{\text{Ovspd}}$  only increases slowly, and the overload protection then dynamically adjusts the remaining elevator command  $u_{\text{elev}}$  to stay below  $n_z^{\text{lim}}$ .

Once the inner-loops are well-tuned, waypoint guidance is enabled. *AtlantikSolar* employs a nonlinear guidance law to generate the lateral acceleration reference  $a_{s,\text{ref}}$  and corresponding roll references  $\phi_{\text{ref}}$  for the UAV. The process uses the current ground speed and heading (Park, Deyst, & How, 2004) along with a look-ahead distance  $L_1$  that is adapted online as outlined in (S. Park, J. Deyst and J. P. How, 2007). The guidance law is integrated into our control structure as described in (Oettershagen et al., 2014). It is combined with an extended version of the Pixhawk (Meier et al., 2015) open-source Total Energy Control System (TECS) which provides altitude and airspeed control. The following custom extensions were implemented in our own TECS variant:

- A *slew rate constraint* on the reference altitude  $h_{\text{ref}}$  allows smoother altitude control at pre-definable climb and sink rates. This is especially important for low propulsion-power to weight ratio UAVs such as *AtlantikSolar*.
- *Passive thermal compliance* has been implemented to cope with up- and downdrafts. In an updraft, the standard TECS implementation will decrease the pitch reference  $\theta_{\text{ref}}$  to decrease the altitude if  $h > h_{\text{ref}}$ . Instead of actively working against thermals, we allow the UAV to gain potential energy from an updraft: Our TECS variant can be configured such that  $\theta_{\text{ref}}$  is fully and only used for airspeed control and  $u_{\text{throt}}$  only for altitude control. When at  $h > h_{\text{ref}}$ , the plane will thus keep  $\theta_{\text{ref}} = \theta_{\text{ref}}(t)$  such that  $v_{\text{air}}(t) = v_{\text{air,ref}}(t)$  and will gradually reduce motor power, potentially gaining altitude for strong thermals.
- *Hard constraints* have been implemented, i.e. full throttle is forced for  $h < h_{\text{min}}$ , and at  $h > h_{\text{max}}$  the controller automatically engages the spoilers (upwards deflected ailerons) for increased descent

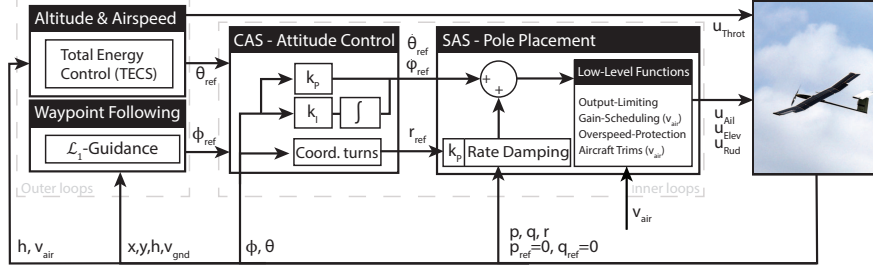


Figure 11: Cascaded control scheme implemented for ETH Zurich’s solar-powered UAVs.

rate and gradually commands a pitch-down and thus maximum descent rate.

The inner PID-based pitch- and roll control loops are executed at a sampling period of  $T_{SAS,CAS} = 0.01s$ , while the high-level (HL) nonlinear guidance and TECS controllers run with  $T_{HL} = 0.05s$ . The full controller requires less than 4% CPU load, 9KB of RAM and 47KB Flash memory and is thus computationally lightweight when compared to other Pixhawk applications (Oettershagen et al., 2014). The controller is designed to be modular, and more sophisticated approaches like model predictive control (Oettershagen et al., 2014) and robust  $H_\infty$ -based controllers (Mosimann, 2014) have been implemented and flown on test planes in addition to the aforementioned PID-baseline inner-loop control solution.

The performance of the control scheme can be analyzed using Figure 12, which shows an early-morning flight in relatively calm air. The first 320s of the left plot demonstrate fully autonomous ( $AP-mode = 5$ ) aircraft operation in constant-altitude loitering. The positive roll angle and yaw change indicate a right-turn, and the periodic variations in the roll angle reference  $\phi_{ref}$  are necessary to provide accurate circle tracking via the nonlinear guidance law in the horizontal wind of  $v_{wind} \approx 2.5\text{ m/s}$ . The automatic throttle variation by TECS keeps the altitude  $h$  within  $\pm 2\text{ m}$  of  $h_{ref}$ . The automatic pitch reference adaptation by TECS tracks the reference airspeed  $v_{air}^{ref} = 8.29\text{ m/s}$  such that  $v_{air} = 8.30\text{ m/s}$  with a very low standard deviation of  $0.1\text{ m/s}$ . Note that higher-level functions such as the passive thermal compliance and the automatic spoiler deployment are demonstrated in section 4.1 and (Oettershagen, Melzer, Mantel, Rudin, Lotz, et al., 2015). The exact tracking performance of the inner loops can be seen best during the autopilot-assisted operation (CAS,  $AP-mode = 2$ ) in  $t = [320\text{ s}, 866\text{ s}]$ . In this mode, the altitude and airspeed are not autopilot-controlled anymore, but only  $\phi_{ref}$  and  $\theta_{ref}$  given by the human safety pilot are tracked. Therefore, at  $t = 320\text{ s}$  the altitude drops and the fluctuations in  $v_{air}$  increase. As shown by the right plot, the roll- and pitch-tracking is very accurate, i.e. no significant bias, scale issue or delay can be noticed. Two internal mechanisms of the controller are exposed in Figure 12: First, the dynamic-pressure gain-scheduling is continuously applied to the control outputs via the airspeed-dependent scaling factor  $f_{GS,q}$ . Second, during the step-like banking commands, the aircraft still manages to achieve the coordinated-turn (body) yaw rate  $r_{ref} = \frac{g \cdot \sin(\phi)}{v_{air}}$  without excessive adverse yaw. Achieving good turn coordination on aircraft with a small rudder, high wingspan and significant battery- and solar-cell-mass distributed along the wing is a significant challenge because of the weakly-damped yaw-dynamics and the strong adverse yaw tendency. On *AtlantikSolar*, we control this issue via an aileron differential of 60% and via significant rudder actuation based on feed-forward and proportional control that aims to track  $r_{ref}$ . However, especially at very low airspeeds around  $8\text{ m/s}$  a small adverse yaw effect persists due to the limited rudder authority. At  $t = 866\text{ s}$ , the pilot switches back to fully manual control mode ( $AP-mode = 0$ ). While the high bank angles were commanded on purpose, both the pitch-variations and the significant deviation in airspeed were not intended by the pilot. These deviations correlate with respective angle of attack changes and are thus a major cause of performance losses.

Overall, Figure 12 shows that the cascaded control scheme of Figure 11 provides very satisfactory guidance- and control-performance despite the inherently hard-to-control slow undamped dynamics of solar-powered high-performance aircraft. In addition to the calm flight conditions of Figure 12, the control scheme has also shown its disturbance-rejection capabilities in long-endurance flights with significant turbulence, thermal

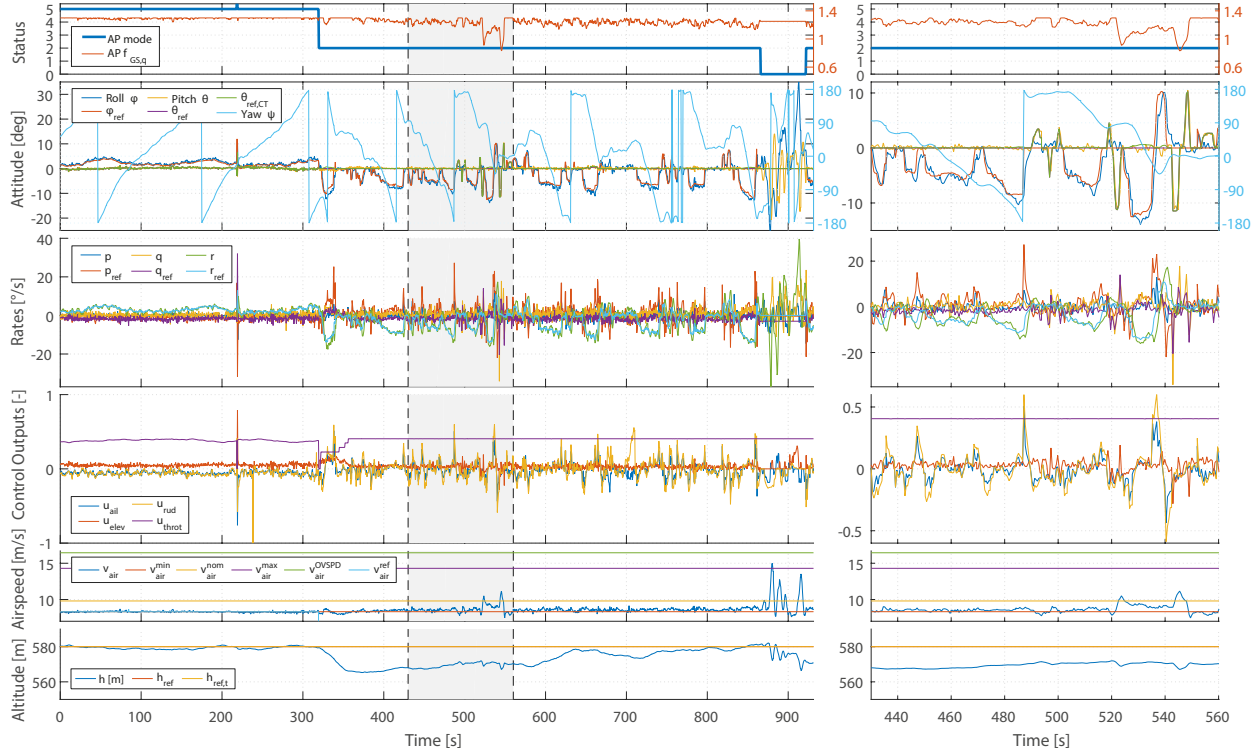


Figure 12: Autopilot-controlled flight of *AtlantikSolar*. The right plot provides more details of the grey patch in the left plot, which (from left to right) shows operation in fully autonomous mode ( $AP\text{-mode} = 5$ ), CAS or autopilot assisted mode ( $AP\text{-mode} = 2$ ) and manual flight mode ( $AP\text{-mode} = 0$ ).

activity and horizontal winds (section 4). As long as no higher-level intelligence is required and the operation happens close to the linearization- or tuning-point, the autopilot will also fly more *economically* than a human pilot: We have observed that in both calm and turbulent flight conditions the autopilot’s better tracking of an aerodynamically optimal reference state leads to a system power consumption decrease of up to 40%.

### 3.3 Preliminary UAV Design Verification

With the detailed system design completed, the *perpetual flight* performance predictions from the conceptual design of section 2 can be verified using lab- or short flight-tests. The decisive metrics verified individually in this section are the solar power income  $P_{\text{solar}}$  and the required output power  $P_{\text{out}}$ , on which the aircraft mass  $m_{\text{tot}}$  has a decisive influence. The goal is to qualify and quantify the respective modeling errors to — if the errors are systematic — allow correcting the very simple conceptual design models to improve the performance prediction in the early design.

#### 3.3.1 Solar Power Income Model

Two different solar power system verification aspects need to be answered: First, is the UAV’s solar power system working properly, and second, how precisely can we actually predict its performance during the conceptual design stage with the limited information available then? Clearly, accurate models are required to answer those questions. Given that this paper’s focus is not on solar power modeling, a separate technical report (Oettershagen, 2017) is released together with this paper to lay the basis for answering these questions. The report introduces and discusses the following models:

- *Full Solar Power Model (FM)*: Usable once the detailed design is complete and the flight path is known, this fully time- and aircraft-state dependent model is accurate enough to detect, understand and mitigate solar power system issues. The FM considers the full aircraft-attitude and -geometry (e.g. wing dihedral and solar cell pitch offsets), considers direct- and diffuse-radiation separately, models the solar module efficiency  $\eta_{\text{sm}}$  as a function of the irradiation level, solar module temperature and the sun radiation’s angle-of-incidence (AoI), and models the MPPT efficiency  $\eta_{\text{mppt}}$  as a function of  $P_{\text{solar}}$ .
- *Conceptual Analysis Model (CAM)*: Usable in the later stages of the conceptual design once the solar module has been chosen, this model assumes a single flat solar module surface and a constant  $\eta_{\text{mppt}}$  but keeps the very important angle-of-incidence correlation of  $\eta_{\text{sm}}$ . It is thus of higher fidelity than the Conceptual Design Model, but can still be used for a detailed performance prediction (see section 5) at a stage when the exact mission conditions (e.g. flight path, wind conditions) are unknown because it assumes a constant horizontal flight attitude.
- *Conceptual Design Model (CDM)*: Usable and used already in the early conceptual design stage (see section 2.3), this model assumes a single, flat and always horizontal solar module surface, a constant MPPT efficiency  $\eta_{\text{mppt}}$  and a constant solar module efficiency  $\eta_{\text{sm}}$  that is only a function of a user specified constant temperature  $T_c$ .

The main results from (Oettershagen, 2017) that are of importance for this paper are, first, that apart from rare MPPT tracking problems in low light conditions the *AtlantikSolar* solar power system works properly: It satisfactorily matches the predictions of the Full Solar Power Model, i.e. generates only 5% less solar power during low- and 3% more solar power during high irradiation conditions. Second, the assessment shows that the CDM overestimates  $P_{\text{solar}}$  by 17%. It is suggested to add the angle-of-incidence dependence of  $\eta_{\text{sm}}$  by using the CAM as early as possible as this reduces the overestimation to 5%. The remaining difference to the FM is caused by horizontal winds and a resulting difference in the aircraft attitude, which can be considered once the flight path is available. On the incoming solar power side, the CAM- and FM-predictions can be considered verified satisfactorily. However, the CDM predictions deviate significantly and cannot be considered verified using the single solar cycle used in (Oettershagen, 2017). This is why section 4.1.2 presents a brief re-assessment of these solar models using the comprehensive 81-hour flight data.

### 3.3.2 Airplane Mass Model

The overall system mass  $m_{\text{tot}}$  has, via Eq. (7), a decisive influence on  $P_{\text{level}}$  and  $P_{\text{out}}$ . As an intermediate verification step, Table 4 therefore compares the masses from the automatic structural sizing approach of section 2.1 to those measured for the final *AtlantikSolar* configuration. Given that this paper and Table 4 focus on characterizing the systematic modeling errors of our approach, but not the effects of a user supplying wrong inputs, we have assumed — for both Table 4 and section 2.3 — the user inputs  $m_{\text{pld}}$  and  $m_{\text{av}}$  to be known perfectly beforehand<sup>1</sup>. Under this assumption, the structural- and solar module mass estimates by the conceptual design model (CDM) deviate by less than 10% and the propulsion- and MPPT-masses deviate by 30% at low absolute error. The batteries are manufactured according to the specification from section 2.3 and their mass is thus approximately correct. Overall, our conceptual design methodology overestimates the aircraft mass by 0.2 kg or 3%. Note that this level of prediction accuracy can only be reached through extensive project experience (Noth, 2008a) and the use of small-scale component level prototypes manufactured for feasibility analysis. In our example, downscaled prototypes of a solar module (0.125 m × 0.75 m size) and of a part of the wing structure (wing chord 0.3 m × wing span 0.5 m) were used to calibrate the scaling constants that determine  $m_{\text{struct}}$  and  $m_{\text{sm}}$  as a function of wingspan, aspect ratio and battery mass.

---

<sup>1</sup>Consider that, as an example of the consequences of a wrong user input, an avionics mass (autopilot, servos, sensors, redundancy battery, wires, mechanical fittings) of only 0.6 kg was estimated during the very early conceptual design phase. The result is an underestimate of  $m_{\text{tot}}$  by 0.49 kg or 7.3%. Through Eqs. (4)-(7)  $P_{\text{out}}$  would have been underestimated by 11.1% and  $T_{\text{exc}}$  and  $T_{\text{cm}}$  would have increased accordingly. This clearly underlines the mass-sensitivity of solar-powered UAV performance and the importance of a precise iterative experience- and prototype-based mass estimation process.

Table 4: Aircraft subsystem masses for the *AtlantikSolar* UAV configuration with  $m_{\text{bat}} = 2.9 \text{ kg}$ ,  $b = 5.6 \text{ m}$ ,  $\lambda = 18.5$  from the conceptual design step (*Estimate*) and after the detailed design phase (*Measured*).

	Measured	Estimate (CDM)	Comment
$m_{\text{pld}}$	0.00 kg	0.00 kg	Fixed user input
$m_{\text{av}}$	1.22 kg	1.22 kg	Fixed user input (592 g avionics, 628 g cables and fittings)
$m_{\text{struct}}$	1.52 kg	1.63 kg	
$m_{\text{prop}}$	0.28 kg	0.37 kg	Includes propeller, gearbox, motor, motor controller
$m_{\text{sm}}$	0.84 kg	0.85 kg	
$m_{\text{mppt}}$	0.12 kg	0.16 kg	
$m_{\text{bat}}$	2.93 kg	2.90 kg	Manufactured according to conceptual design specification
<b><math>m_{\text{tot}}</math></b>	<b>6.92 kg</b>	<b>7.12 kg</b>	

### 3.3.3 Output Power Model

While the mechanical level flight power of Eq. (7) can be estimated through glide rate tests, a way to incorporate the important propulsion efficiency contribution and to thus directly retrieve the electric level flight power of Eq. (4) is to set the aircraft into constant-altitude loitering mode while, as described in (Oetershagen, Melzer, Mantel, Rudin, Lotz, et al., 2015), performing an airspeed sweep over  $v_{\text{air}} = [7.4 \text{ m/s}, 13.5 \text{ m/s}]$  and measuring the  $P_{\text{out}} = f(v_{\text{air}})$  relationship. The measured power curve is depicted in Figure 13. To diminish the effects of turbulent air, the data was gathered shortly after sunrise before the thermal updraft, downdraft and gust activity usually sets in. Nevertheless, significant noise remains in the raw data. For every  $v_{\text{air}}$ -point,  $P_{\text{out}}$  was therefore averaged over an interval of  $T = 200 \text{ s}$  to remove errors due to noisy airspeed-, current- and voltage-sensor readings and the coupling of altitude errors into the required motor power via the altitude-control law of section 3.2.3. An absolute minimum of  $P_{\text{out}} = 39.7 \text{ W}$  at  $v_{\text{air}}^{\text{opt}} = 8.3 \text{ m/s}$  can be identified. However, winds and turbulence will cause airspeed-tracking errors and will also generally require flight at increased airspeed. A more appropriate airspeed interval to choose is thus  $v_{\text{air}} = [7.9 \text{ m/s}, 8.8 \text{ m/s}]$ . In this interval, the measured power consumption is still  $P_{\text{out}} \leq 41.8 \text{ W}$ , and thus equal to or below the power consumption predicted by our conceptual *design* methodology based on Eqs. (4)-(8). This confirmation of the power requirement via the measurement means that — on the output power side — the predicted 24-hour flight capability and excess time are verified. Note that once a measured power curve is available it can be used as a direct user input in the *analysis* part of our design framework, thereby increasing the framework’s performance prediction accuracy.

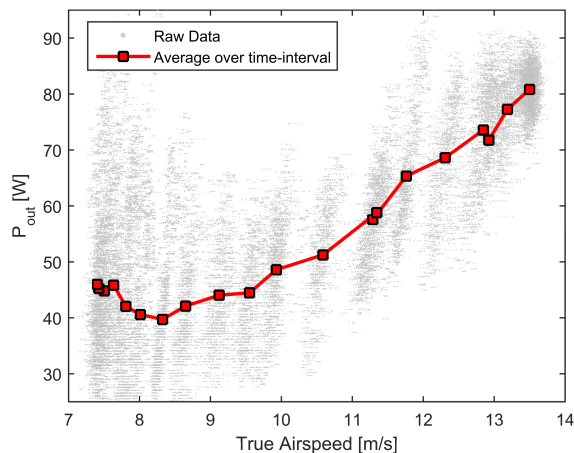


Figure 13: *Power curve*, i.e. the total required level power  $P_{\text{out}}$  vs. the true airspeed  $v_{\text{air}}$ , measured in constant-altitude loiter mode and averaged over  $T = 200 \text{ s}$  intervals for each plotted point.

However, an important lesson learned was that the modeling through Eqs. (4)-(8) only provides an absolute lower limit for  $P_{\text{out}}$ . These equations assume undisturbed flight at minimum sink airspeed, whereas in reality deviations in airspeed and attitude or even downdrafts cannot be avoided, and the propulsion efficiency  $\eta_{\text{prop}}$  assumed in Table 1 is also not straightforward to reach. The low power consumption from Figure 13 was for example only reached after significant propulsion system optimization: The propeller was completely re-designed and wind-tunnel tested to optimize it for *AtlantikSolar*'s specific level-flight conditions, and multiple hardware-iterations on the motor were necessary to select the best motor constant (e.g.  $k_V$ ) and to reach the predicted power requirement. The finally selected *AtlantikSolar* motor with  $k_V = 470 \text{ RPM/V}$  provides  $P_{\text{elec}}^{\text{max}} = 420 \text{ W}$  and reaches  $\eta_{\text{motor}} \approx 80.6 \%$  in level flight.

## 4 Flight Results

During the challenging three years of design, development and sometimes perilous flight testing, a total of 239 flight hours and 72 flights have been accumulated with the three *AtlantikSolar* UAVs designed and built so far. The initial design and long-endurance flights up to 12 hours with the *AtlantikSolar* prototype (*AS-P*) and first version (*AS-1*) are presented in (Oettershagen, Melzer, Mantel, Rudin, Lotz, et al., 2015). Typical real-world applications are covered in (Oettershagen, Stastny, et al., 2015). For example, the *AtlantikSolar* prototype is equipped with the sensor pod of section 3.1.5 and used for long-endurance search-and-rescue research projects via aerial surveillance and its victim detection capabilities. In addition, long-endurance aerial mapping in winter conditions is described. A more recent 28-hour continuous solar-powered flight of *AtlantikSolar* AS-2 that represented its first *perpetual flight* is discussed in (Oettershagen et al., 2016).

This section discusses the culmination of previous work and the design efforts of the previous sections: The continuous 81-hour solar-powered flight of *AtlantikSolar* AS-2 from July 14<sup>th</sup> – 17<sup>th</sup> 2015 that covered 2338 km of ground-distance<sup>2</sup>. At the time of writing, this flight represents the current world record in flight endurance for all aircraft below 50 kg total mass. Although not filed as a record at the Fédération Aéronautique Internationale (FAI)<sup>3</sup>, it is currently also the second-longest flight of any Unmanned Aerial Vehicle, the third-longest flight of any solar airplane, and the fifth longest flight of any aircraft both manned or unmanned. In conjunction with this paper, the complete flight logs have been released at (Oettershagen, 2016a). In comparison to previous *perpetual flight* capable aircraft, we achieve *perpetual flight* at significantly lower overall system mass and size than (QinetiQ, 2010) and with significantly higher energetic safety-margins than (Cocconi, 2005; Noth, 2008a).

### 4.1 A Continuous 81-hour Solar-Powered Flight

#### 4.1.1 Flight Description

The continuous solely solar-powered flight of 81 hours 26 minutes 14 seconds was performed by *AtlantikSolar* AS-2 from July 14<sup>th</sup> to July 17<sup>th</sup> 2015 at  $\varphi_{\text{lat}} = 47.6^\circ$  in Rafz, Switzerland. The airplane was launched in manual mode and the landing was executed in autopilot-assisted (CAS) mode. Overall 99.9% of the flight were performed in either fully autonomous or autopilot-assisted mode and 92% in fully autonomous mode<sup>4</sup>. As common for LALE-UAVs aiming for perpetual endurance, the flight strategy was to fly low at constant altitude to reduce power consumption. Because of the limited flight space available the aircraft was set into loitering mode. The flight conditions are summarized in Table 5. The first three days showed excellent flight conditions, i.e. mostly clear sky or marginal high altitude clouds that allow a direct comparison of the flight

<sup>2</sup>A video of the 81-hour flight is available at [https://www.youtube.com/watch?v=8m4\\_NpTQn0E](https://www.youtube.com/watch?v=8m4_NpTQn0E), and a video summarizing aerial sensing and mapping applications is located at <https://www.youtube.com/watch?v=OUyHZUQXfPo>. Further videos can be accessed through our YouTube channel at <https://www.youtube.com/user/AtlantikSolar>

<sup>3</sup>A list of FAI-registered records is available at [www.fai.org/records](http://www.fai.org/records). However, many flights such as the previous duration record in the sub 50 kg class (Cocconi, 2005) are not registered with FAI. The 81-hour flight of *AtlantikSolar* AS-2 was not registered with FAI because of scheduling reasons.

<sup>4</sup>A portion of the autopilot-assisted flight time was used for training an additional RC safety-pilot

data to the models of section 3.3.1. Horizontal winds were calm on the second and third day, but the first day and especially the thunderstorm on the third day posed significant challenges.

Table 5: Clouds, horizontal winds and thermal activity during the 81-hour flight. The wind direction indicates in which direction (North = 0°, clockwise positive, i.e. as for the yaw angle) the wind is flowing. Morning represents 4am-10am, noon 10am-4pm, evening 4pm-8pm and night 8pm-4am local solar time.

Date	Time	Cloud cover	Horizontal wind	Thermal activity
July 14 <sup>th</sup> (Day 1)	Morning	Clear sky	5–7 m/s, NE (65°)	medium
	Noon	Few cumulus	7–8 m/s, E(80°)	strong
	Evening	Few cumulus	4–6 m/s, E(85°)	medium
	Night	Clear sky	1–4 m/s, S(170°)	medium evening thermal (11pm)
July 15 <sup>th</sup> (Day 2)	Morning	Clear sky	1–3 m/s, SW (230°)	medium
	Noon	Clear sky	2–4 m/s, varying dir.	strong
	Evening	Clear sky	1–3 m/s, NW(-60°)	medium
	Night	Clear sky	1–2 m/s, varying dir.	none
July 16 <sup>th</sup> (Day 3)	Morning	Clear sky	1–2 m/s, W (250°)	weak
	Noon	Few cirrus	2–3 m/s, varying dir.	strong
	Evening	Clear sky	3–5 m/s, E(110°)	medium
	Night	Clear sky	1–3 m/s, varying dir.	weak evening thermal (10pm)
July 17 <sup>th</sup> (Day 4)	Morning	Clear sky	2–3 m/s, NE (50°)	weak
	Noon	Cirrus & cumulus	3–8 m/s, NE(50°)	medium
	Evening	Thunderstorm	7–17 m/s, N(0°)	N/A

Figure 14 presents the results of the complete 81-hour flight. The power plot clearly shows the three transitions between daytime and nighttime. After launch with  $\sigma_{\text{bat}} = 63\%$  at 8.00 h local solar time (9:32am local time) on the first day, the favorable conditions (Table 5) and especially the strong north-east wind allow the measured solar power income to exceed the prediction by the conceptual design and analysis models. Due to the level-flight power consumption of  $P_{\text{out}} \approx 50\text{ W}$ , the batteries are charged with up to  $P_{\text{bat}}^{\text{exp}} = 165\text{ W}$ . At  $t = 9.27\text{ h}$  local solar time and  $\sigma_{\text{bat}} = 88\%$ , the MPPTs begin to reduce their output power to prevent battery damage. At  $t = 10.55\text{ h}$ , the batteries are fully charged. The MPPTs do not charge the battery anymore but do still supply the necessary motor power of up to  $P_{\text{out}} = 150\text{ W}$  to keep the altitude e.g. during the thermal downdraft at  $t = 11.37\text{ h}$ . The battery discharge begins ( $\sigma_{\text{bat}} \leq 99\%$ ) at  $t = 18.48\text{ h}$  solar time, and the horizontal winds now cause  $P_{\text{solar}}^{\text{exp}}$  to be below the conceptual design and analysis predictions. During the night, the solar power income naturally decreases to zero and thus  $P_{\text{bat}}^{\text{exp}} = -P_{\text{out}}^{\text{exp}}$ .

The sunrise on the second day occurs at  $t_{\text{sr}} = 28.4\text{ h}$  solar time (4.4h on that day) and the minimum state-of-charge is  $\sigma_{\text{bat}} = 41\%$  at  $t = 29.79\text{ h}$ . The first night was completed with sufficient energetic margins. The tracking plot of Figure 14 however reveals a partial MPPT failure between  $t = 30.97\text{ h}$  and  $t = 34.57\text{ h}$  that causes  $P_{\text{solar}}^{\text{exp}}$  to fall up to 35 W or 23% below the full model prediction and also delays the battery charging process. During the afternoon and evening, the solar power system exhibits nominal behavior. As visible in Figure 15 (center), and despite beginning shadowing of the solar modules, we have  $P_{\text{solar}}^{\text{exp}} > P_{\text{solar}}^{\text{model}}[\text{CAM}]$  due to winds of 3–5 m/s in north west direction for  $t > 41.67\text{ h}$ . The second night, third day and night, and the fourth morning show nominal system behavior in good irradiation conditions and calm winds. The energetic performance for these days is shown in Table 7. However, during the afternoon and evening of the fourth day significant cumulus and thunderstorm clouds lead to a decreased  $P_{\text{solar}}$ . Figure 15 (right) also shows that  $v_{\text{wind}}$  has increased to up to 17 m/s. The airspeed  $v_{\text{air}}$  (typically 8.6 m/s) is increased to compensate  $v_{\text{wind}}$ , throttle and thus altitude are increased to gain potential energy, and the aircraft is flown in autopilot-assisted mode — all to avoid a drift-off of the aircraft. Atmospheric turbulence close to the thunderstorm and flight at high airspeed both challenge the flight controller. The flight conditions increase power consumption and cause an earlier discharge at  $t = 88.67\text{ h}$ . However, during the autopilot-assisted landing in calmer conditions

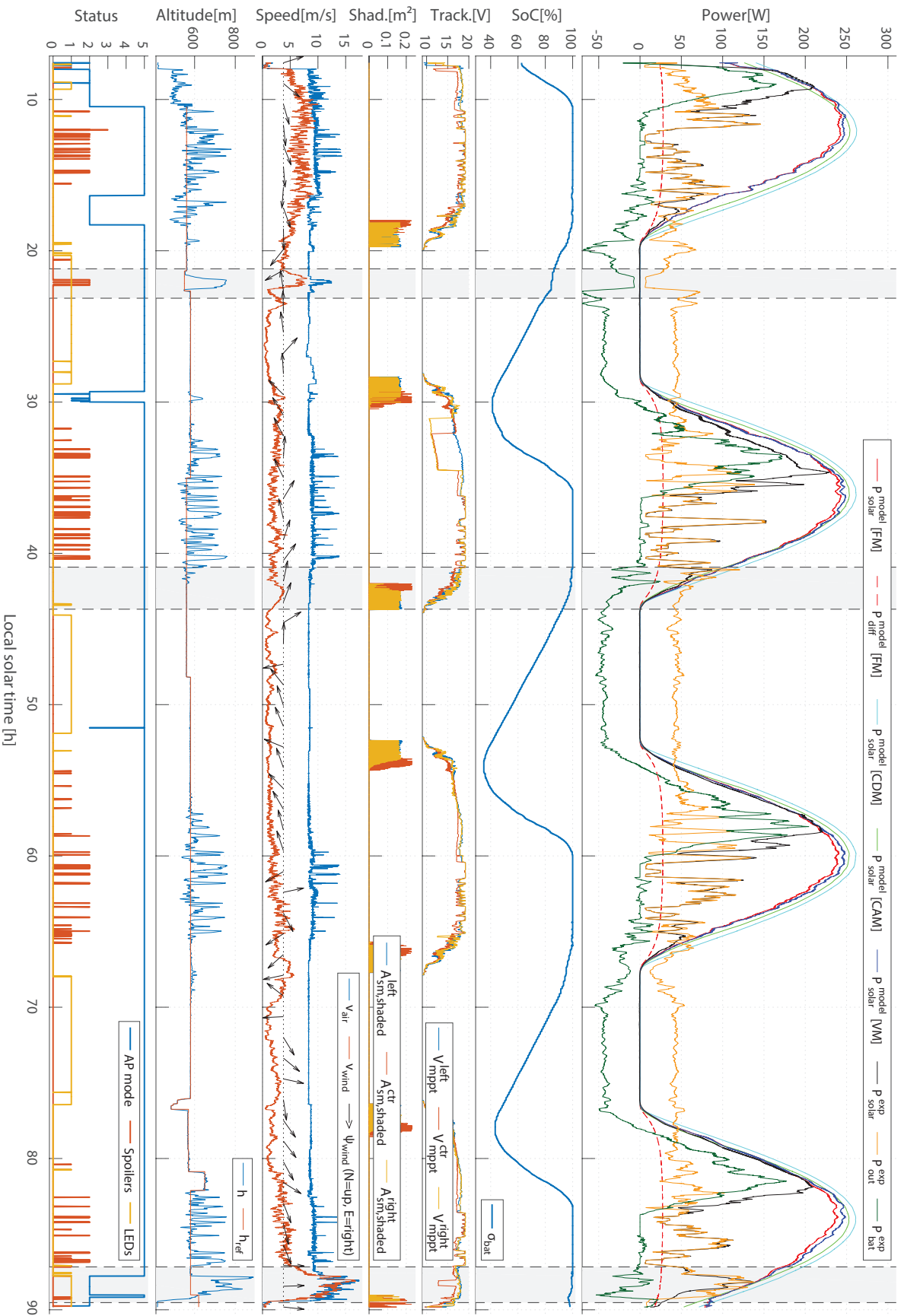


Figure 14: Results from the 81-hour continuous solar-powered flight of *AtlantikSolar* AS-2 from July 14<sup>th</sup>-17<sup>th</sup> 2015. The data is sampled at 2Hz and a two-sided moving average filter is applied to all data except for the Status and Shading plots. The semi window length of the filters is 1000 samples for the power plot and 100 samples for all others. The three grey patches represent the detailed plots of Figure 15. In the status plot, the AP mode flag is [0=MAN, 1=SAS, 2=CAS, 5=AUTO], the Spoiler flag is [0=OFF, 1=ON(MAN), 2=ON(AUTO)], the LED flag is [0=OFF, 1=ON].

at  $t = 89.44$  h (6:58pm local time) on July 17<sup>th</sup>, the batteries are still at  $\sigma_{\text{bat}} = 96\%$ . Note that the landing was initiated because the flight endurance goals had been fulfilled, but from an energetic perspective the flight could have continued even under these circumstances.

#### 4.1.2 Flight Analysis

Before assessing the actual performance metrics in section 4.2, this section performs a separate analysis for each of the two components that determine the performance metrics, namely the incoming power  $P_{\text{solar}}$  and the required power  $P_{\text{out}}$ . For the power income assessment, we apply the same methodology as in (Oetershagen, 2017) and just use the three solar cycles of the 81-hour flight instead of just one solar cycle. When omitting the intervals of MPPT tracking failure during the second day as well as the phases of strong cloud cover on the fourth day, we obtain Table 6. The results for the model accuracy found in section 3.3.1 are largely confirmed: The average errors are similar for the conceptual design and analysis models, but the full model now slightly overestimates ( $\hat{e}_{P_{\text{solar}}}^{\text{avg}} = 2.45\%$ ) the power income instead of underestimating it. The significant CDM prediction error again confirms that, as further discussed in section 4.2.2, the respective solar income performance results need to be handled with care.

Table 6: Estimation errors of the presented solar power models during the 81-hour flight. The subscript  $\mathcal{F}$  in  $P_{\text{solar},\mathcal{F}}$  again denotes that the underlying data is pre-filtered (using the same filter as Figure 14) to allow a meaningful comparison between the attitude-dependent FM and the attitude-independent CDM and CAM. The application of the filter only influences the RMS errors.

Name	CDM	CAM	FM	Flight Data
Application	Conc. Design	Conc. Analysis	Full model	
$P_{\text{solar}}^{\text{avg}}$	89.99 W	79.55 W	77.13 W	75.29 W
$\hat{e}_{P_{\text{solar}}}^{\text{avg}}$	19.52 %	5.65 %	2.45 %	—
$\hat{E}_{P_{\text{solar},\mathcal{F}}}^{\text{RMS}}$	18.68 W	8.7 W	4.08 W	—
$\hat{e}_{P_{\text{solar},\mathcal{F}}}^{\text{RMS}}$	24.81 %	11.55 %	5.42 %	—

Having assessed the solar power income, we now focus on the required output power  $P_{\text{out}}$ . Figure 14 shows that during phases of stable atmospheric stratification (nights and early morning) we have good reference tracking, i.e.  $h \approx h_{\text{ref}}$  and  $v_{\text{air}} \approx v_{\text{air}}^{\text{ref}}$ , and the required output power is very even. A more direct comparison is given in Figure 16, which plots  $P_{\text{out}}$  against the solar time over multiple days. We find<sup>5</sup> that during the

- *night and early morning* (11pm–7am, all solar times), we have  $P_{\text{out}}^{\text{avg}} = 43.9$  W at a standard deviation (computed from the unfiltered  $P_{\text{out}}$ ) of only  $\sigma = 6.83$  W.
- *day* (7am–7pm), we retrieve  $P_{\text{out}}^{\text{avg}} = 54.37$  W at  $\sigma = 26.5$  W due to increased thermal activity that starts two hours after sunrise and is indicated by large altitude changes (not suppressed due to the flight controller’s passive thermal compliance, see section 3.2.3).
- *evening and early night* (7pm–11pm), the small  $h$ - and  $v_{\text{air}}$ -fluctuations indicate low turbulence levels. However, an unexpected drop to  $P_{\text{out}}^{\text{avg}} = 35.7$  W at  $\sigma = 9.97$  W is caused by a significant evening thermal on the first day (Figure 15, left) and a weaker one on the third evening. The former updraft starts at  $t = 21.6$  h while the UAV operates fully autonomously and with position lights. It lifts the UAV to  $h_{\text{max}}$ , upon which the UAV automatically engages its spoilers and even has to pitch down to obey  $h_{\text{max}}$ . After one hour of unpowered flight  $h = h_{\text{ref}}$  is reached again.

Overall, we retrieve  $P_{\text{out}}^{\text{avg}} = 41.6$  W over the full nighttime flight from 8pm–6am solar time. This very

<sup>5</sup>This observed daily development of the atmospheric turbulence and thermal activity also confirms the daily stratification cycle found in typical *boundary layer meteorology* literature (Stull, 1988)

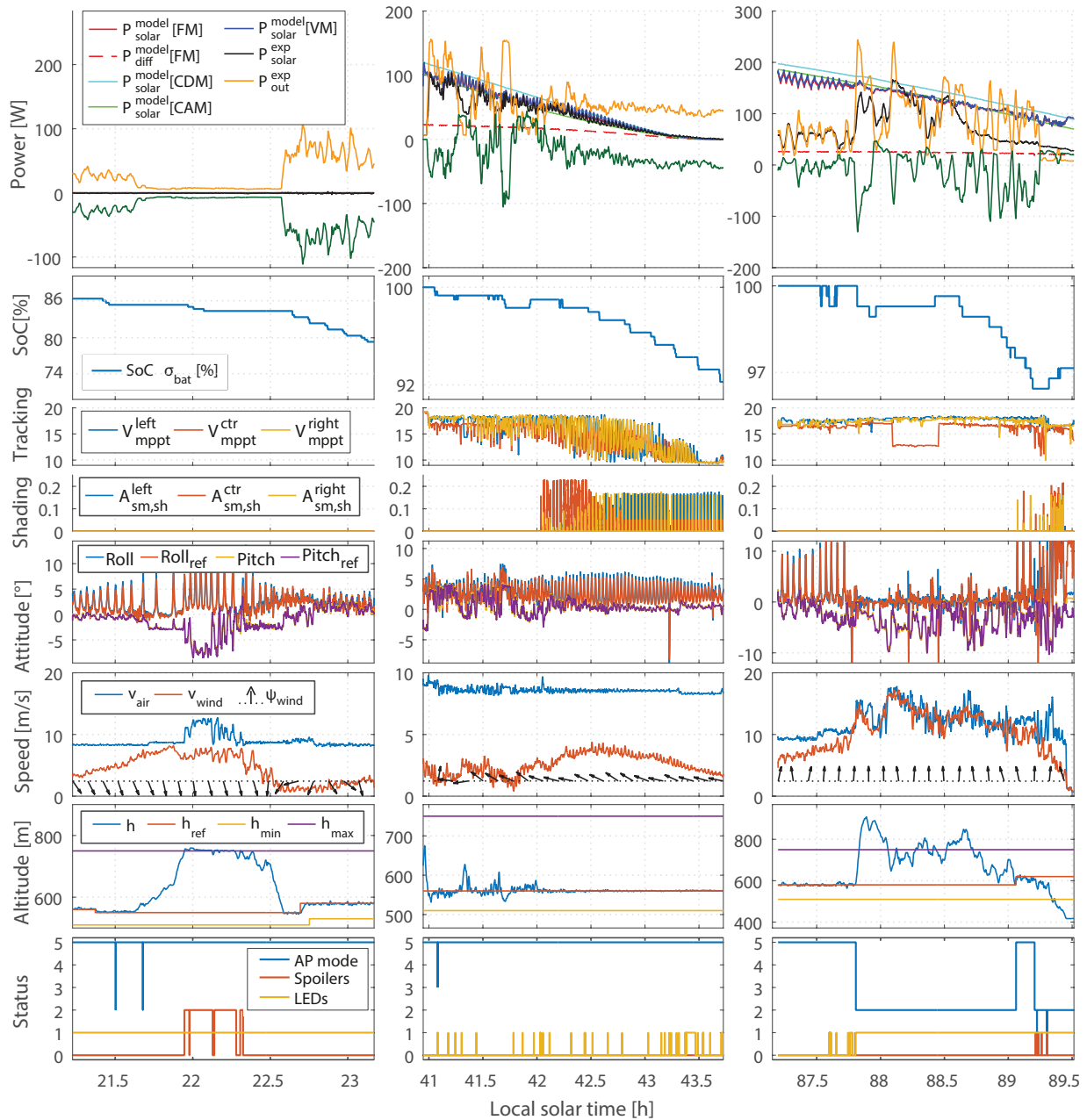


Figure 15: Detailed flight results from the 81-hour continuous solar-powered flight. Left: First night, Center: Second evening, Right: Fourth evening. The data is calculated or measured at 2 Hz and a two-sided moving average filter with a semi window length of 50 samples is applied to all data except for the Status and Shading plots. In the status plot, the AP mode flag represents [0=MAN, 1=SAS, 2=CAS, 5=AUTO], the Spoiler flag represents [0=OFF, 1=ON(MAN), 2=ON(AUTO)], the LED flag represents [0=OFF, 1=ON].

important result confirms that the early-morning power measurements of section 3.3.3 also hold throughout the whole night, and thereby also confirms the predicted  $P_{\text{out}} = 41.8 \text{ W}$  of section 2.3 again. During the day (7am–7pm), the thermal activity thus increases  $P_{\text{out}}^{\text{avg}}$  by 30.7% with respect to the nighttime power consumption. This is despite the fact the vertical air movement in the atmosphere has to obey mass conservation (Stull, 1988) and the fact that the aircraft makes passive use of thermal updrafts (section 3.2.3). The *reason* are the flight controller’s altitude restrictions, i.e. the fact that the passive thermal compliance cannot use updraft energy that would lift the aircraft above  $h_{\text{max}}$ , but has to compensate the full downwards air movement in a strong downdraft to guarantee that  $h \geq h_{\text{min}}$ . The *consequences* for solar-powered UAVs are in general not as severe as for non-solar-powered UAVs because of the (excess) power income during the afternoon. However, downdrafts that occur towards the evening at low  $P_{\text{solar}}$  often result in  $P_{\text{out}} > P_{\text{solar}}$ , and the resulting battery discharge can then afterwards only be compensated with a limited charge power at high  $\sigma_{\text{bat}}$  (section 2.1). Two *mitigations* are possible: First, in flight, an active thermal tracking algorithm that helps to avoid downdrafts and finds thermal updrafts is considered for future research. Second, for the conceptual design and analysis environment, a simple factor that scales  $P_{\text{level}}$  linearly with time towards mid-day has been integrated and is assessed in section 4.2 and Table 7 (CAM/T model). This factor models the changes in the charge margin  $T_{\text{cm}}$  due to the increased power consumption under thermal activity.

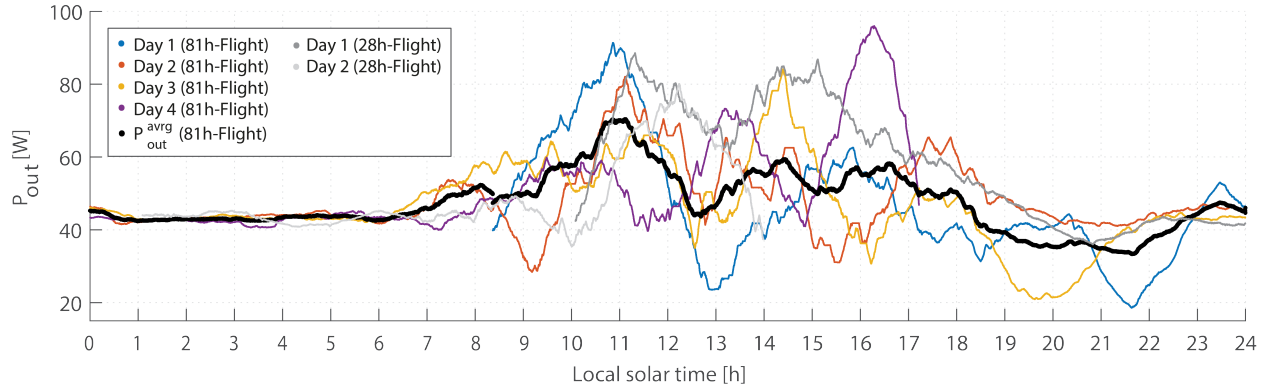


Figure 16: Per-day power consumption  $P_{\text{out}}$  during the 81-hour flight. The 28-hour flight data is also given. A two-sided moving average filter of window length 1 hour was applied to the data.

## 4.2 Performance Metrics: Flight Testing and Model

The performance metrics introduced in section 2.2 give a clear picture of the energetic margins a solar-powered UAV provides with respect to *perpetual flight*. They are summarized for *AtlantikSolar*’s 81-hour flight, the 28-hour flight and the conceptual design and analysis models in Table 7.

### 4.2.1 Performance Metrics Achieved During Flight Testing

During the 81-hour flight, the minimum state-of-charge ranges between 35% and 43.3%. The deviations are mostly caused by evening thermals, where the first and third day (Figure 16) are characterized by net updraft and the second day by net downdrafts in the evening. Thus, while the arithmetic mean is  $\sigma_{\text{bat}}^{\text{min}} = 39.9\%$  ( $T_{\text{exc}} = 6.82 \text{ h}$ ), we estimate the actual mean without evening thermals to be around  $\sigma_{\text{bat}}^{\text{min}} = 37\%$  ( $T_{\text{exc}} = 6.32 \text{ h}$ ). A similar  $\sigma_{\text{bat}}$  is retrieved for the 28-hour flight. Table 7 also shows that the sunrise and sunset times  $t_{\text{sr}}$  and  $t_{\text{ss}}$  have slightly shifted and thus explains the moderately lower  $\sigma_{\text{bat}}^{\text{min}}$  during the 81-hour flight. For both flights,  $t_{\text{eq}}^{\text{sr}}$  occurs ca. 2 hours after sunrise, and  $t_{\text{eq}}^{\text{ss}}$  occurs 1–2 hours before sunset. The charge margins  $T_{\text{cm}}$  and  $T_{\text{cm}}^{90\%}$  depend on the times of charge  $t_{\text{fc}}^{90\%}$  and  $t_{\text{fc}}$  as well as the power equality time  $t_{\text{eq}}^{\text{ss}}$ , all of which heavily depend on the thermal activity and thus vary significantly. As an example, the low thermal activity during the fourth morning leads to a fast charging process, while the thermal downdrafts during the second day lead to an early discharge. On average, the batteries are fully charged at  $t_{\text{fc}} = 11.91 \text{ h}$  solar time (even earlier if one includes the 28-hour flight) and thus before the solar maximum. Therefore,

Table 7: Performance metrics and characteristic solar times (Figure 3) for the two multi-day endurance flights and the conceptual models without (CDM/CAM) and with (CAM/T) the thermal-induced power consumption increase of section 4.1.2. For the second day of the 28-hour flight, the charge margins are calculated using  $t_{\text{eq}}^{\text{ss}}$  of the first day. Braces indicate unreliable data, for  $t_{\text{fc}}^{90\%}$  and  $t_{\text{fc}}$  because the aircraft was launched at arbitrary state-of-charge  $\sigma_{\text{bat}}$  on that day, and for  $t_{\text{eq}}^{\text{ss}}$ ,  $T_{\text{cm}}$  and  $T_{\text{cm}}^{90\%}$  because of the storm and intense cloud cover on the last day. The calculated mean does not incorporate this less-reliable data.

		Performance Metrics				Characteristic solar times					
		$\sigma_{\text{bat}}^{\text{min}} [\%]$	$T_{\text{exc}} [\text{h}]$	$T_{\text{cm}} [\text{h}]$	$T_{\text{cm}}^{90\%} [\text{h}]$	$t_{\text{sr}} [\text{h}]$	$t_{\text{eq}}^{\text{sr}} [\text{h}]$	$t_{\text{fc}} [\text{h}]$	$t_{\text{fc}}^{90\%} [\text{h}]$	$t_{\text{eq}}^{\text{ss}} [\text{h}]$	$t_{\text{ss}} [\text{h}]$
Flight (81h)	Day 1	N/A	N/A	N/A	N/A	N/A	N/A	(10.55)	(9.40)	18.48	19.70
	Day 2	41.3	6.96	5.46	6.80	4.19	6.22	12.21	10.87	17.67	19.76
	Day 3	35.0	5.93	6.22	7.40	4.26	6.12	11.95	10.77	18.17	19.76
	Day 4	43.3	7.57	(5.13)	(6.61)	4.31	6.00	11.58	10.10	(16.71)	N/A
	<i>Mean</i>	<i>39.9</i>	<i>6.82</i>	<i>6.20</i> <sup>6</sup>	<i>7.53</i>	<i>4.25</i>	<i>6.11</i>	<i>11.91</i>	<i>10.58</i>	<i>18.11</i>	<i>19.74</i>
Sim. (81h)	CDM	39.2	6.63	7.74	9.12	4.35	5.58	10.75	9.39	18.51	19.74
	CAM	36.9	6.27	6.01	8.04	4.35	5.97	12.10	10.09	18.13	19.74
	CAM/T	36.9	6.27	5.86	7.93	4.35	5.97	12.23	10.20	18.13	19.74
Flight (28h)	Day 1	N/A	N/A	N/A	N/A	N/A	N/A	(12.59)	(11.27)	18.80	19.92
	Day 2	41.3	7.35	7.53	8.81	4.02	6.00	11.27	9.99	N/A	N/A
Sim. (28h)	CDM	41.2	6.97	8.11	9.48	4.18	5.44	10.54	9.17	18.65	19.92
	CAM	38.8	6.59	6.37	8.41	4.18	5.83	11.88	9.85	18.26	19.92
	CAM/T	38.7	6.59	6.23	8.28	4.18	5.83	12.01	9.98	18.26	19.92

more than 50% of the daily solar energy remains as a margin. The respective charge margins for the 81-hour flight are  $T_{\text{cm}}^{90\%} = 7.53$  h and  $T_{\text{cm}} = 6.20$  h. The charge rate to  $\sigma_{\text{bat}} = 90\%$  (at which perpetual flight is still feasible) is higher than to full charge because of the implemented battery current limitation at high  $\sigma_{\text{bat}}$ .

Overall, the average performance metrics of  $T_{\text{exc}} = 6.82$  h,  $T_{\text{cm}} = 6.20$  h and  $T_{\text{cm}}^{90\%} = 7.53$  h indicate solid energetic margins that provide increased *perpetual flight* robustness against clouds, atmospheric turbulence or downdrafts. The mean charge margin (considering both the 28-hour and 81-hour flights) is nearly equal to the mean excess time. This verifies that the novel conceptual design approach of section 2 does not only lead to higher, but furthermore to well-balanced energetic margins. In comparison to previous solar-powered UAV designs, the excess time, charge margin and minimum state-of-charge  $\sigma_{\text{bat}}^{\text{min}} = 39.9\%$  are nearly an order-of-magnitude improvement: For example the SkySailor UAV (Noth, 2008a) provided less than 3 hours of charge margin, and approached battery depletion with only  $\sigma_{\text{bat}}^{\text{min}} = 5.8\%$  remaining. The SoLong UAV (Cocconi, 2005) on the other hand resorted to active tracking of thermal updrafts (Noth, 2008b) with human pilots to gather enough incoming energy. Despite not implementing such techniques, *AtlantikSolar* clearly provides more robust *perpetual flight* than all prior low-altitude solar-powered UAV designs. The central goal of the corresponding research and this paper is thus fulfilled.

The significant step forward is made possible through various *AtlantikSolar* design improvements. A first-order analysis can be performed by ‘transforming’ *AtlantikSolar* (AS) back to SkySailor’s (SS) technological parameters using the data in (Noth, 2008a): Without the new battery system ( $e_{\text{bat}}^{\text{AS}} = 251$  Wh/kg,  $e_{\text{bat}}^{\text{SS}} = 240$  Wh/kg) and solar modules ( $\eta_{\text{sm}}^{\text{AS}} = 23.7\%$ ,  $\eta_{\text{sm}}^{\text{SS}} = 16.9\%$ ) only  $\sigma_{\text{bat}}^{\text{min}} = 32.5\%$  and  $T_{\text{cm}} = 5.2$  h are reached (Figure 20). The thorough design process outlined in this paper also plays a key roll: To analyze this, we plug the known  $m_{\text{tot}}$ ,  $A_{\text{wing}}$  and level flight power consumption ( $P_{\text{out}}^{\text{AS}} = 41.8$  W,  $P_{\text{out}}^{\text{SS}} = 18.1$  W) into Eqs. (4,7) and  $P_{\text{prop}} = P_{\text{level}}/\eta_{\text{prop}}$ . Neglecting relative differences in  $P_{\text{av}}$  and  $P_{\text{pld}}$ , the comparison shows a 23.7% lower aerodynamic- ( $C_L^{3/2}/C_D$ ) or propulsion efficiency ( $\eta_{\text{prop}}$ ) for SkySailor. As Figure 20 indicates,

<sup>6</sup>Note that in order to include data from three days instead of just two, the mean  $T_{\text{cm}}$  (and  $T_{\text{cm}}^{90\%}$  equivalently) for the 81-hour flight are calculated as the difference between the mean characteristic times, i.e.  $T_{\text{cm}} = t_{\text{eq}}^{\text{ss}} - t_{\text{fc}}$ , and not as the mean of the pre-calculated charge margins over the different days.

such a propulsion efficiency change reduces  $T_{\text{exc}}$  by 54% and  $T_{\text{cm}}$  by 13%, yielding  $\sigma_{\text{bat}}^{\text{min}} = 13.5\%$  and  $T_{\text{cm}} = 4.4$  h. The remaining difference to the SkySailor performance margins is likely due to aircraft scaling effects, different atmospheric conditions or just measurement errors. Overall, the novel conceptual design process, the specific design choices of section 2 (e.g. aspect ratio of  $\lambda^{\text{AS}} = 18.5$  vs.  $\lambda^{\text{SS}} = 12.5$ ) and the design approaches of section 3 (e.g. a span loader concept and an extensively optimized propulsion system) have resulted in a highly optimized system and are thus responsible for a majority of the *perpetual flight* performance margin increases achieved with the *AtlantikSolar* UAV.

## 4.2.2 Accuracy of the conceptual design and analysis models

The measured performance metrics provide the first opportunity to perform a system-level verification of our conceptual design and analysis framework. The CDM, CAM and CAM/T solar power models produce relative errors in  $T_{\text{exc}}$  and  $\sigma_{\text{bat}}^{\text{min}}$  of -1.7%, -7.5% and -7.5% (0.7, 3.0 and 3.0 percent points for  $\sigma_{\text{bat}}^{\text{min}}$ ) when compared to the measured arithmetic mean of  $\sigma_{\text{bat}}^{\text{min}} = 39.9\%$ . However, as discussed in section 4.1, the true mean without thermal updrafts in the evening may very well lie lower, and thus the achieved modeling errors can be considered very low. In contrast, the errors on the charge margins are significantly higher: As indicated by sections 3.3.1 and 4.1.2, the CDM model overestimates  $T_{\text{cm}}$  by 24.8% and the CAM and CAM/T models slightly underestimate  $T_{\text{cm}}$  (-3.1% and -5.5% respectively). The estimate for  $T_{\text{cm}}^{90\%}$  shows relative errors of 21.1%/6.8%/5.3% respectively.

Overall, the verification shows that when using the conceptual *design* methodology (the first component of our framework), the solar-powered UAV designer needs to expect substantial prediction errors. These errors are not of conceptual nature, but exist because central UAV characteristics are either uncertain (e.g. mass) or not available (e.g. angle-of-incidence-dependence of  $\eta_{\text{sm}}$ , exact  $P_{\text{out}}$ ) during this early design stage. The design process of solar-powered UAVs is clearly of iterative nature, and the assessments of this section show that while it has not been considered in previous work such as (Leutenegger et al., 2010), the above information should be considered as early as possible in the design stage. Our conceptual *analysis* approach (the second component of our framework) does exactly that: Used with the CAM/T model, it allows a prediction - on the conservative side - of  $\sigma_{\text{bat}}^{\text{min}}$  to within 1–3 percent points and  $T_{\text{exc}}$  to within 0.55 h. The charge margins  $T_{\text{cm}}$  and  $T_{\text{cm}}^{90\%}$  show errors of less than 5.5%<sup>7</sup>. All in all, the prediction accuracy of the conceptual analysis framework is sufficient to accurately predict solar-powered UAV performance and their energetic margins with respect to *perpetual flight*. That is especially true when considering the significant inter-day variation of the measured performance metrics in Table 7:  $\sigma_{\text{bat}}^{\text{min}}$  varies up to 8.3 percent points,  $T_{\text{exc}}$  up to 1.64 h and  $T_{\text{cm}}$  up to 0.76 h. Our conceptual analysis framework therefore allows performance metric predictions with an error on par or even below the measured inter-day performance metric variations.

## 5 Performance Outlook

Given the significantly improved performance margins found before, this section provides an overview over what exact performance can be expected from the *AtlantikSolar* UAV and similar solar-powered high performance UAVs over a range of realistic operating conditions and with first sensing payloads. In contrast to section 2.4, we here rely on the accurate conceptual *analysis* framework (the CAM) which uses flight data such as  $P_{\text{out}}$  recorded during the *AtlantikSolar* 81-hour flight. The results discussed here represent the current state-of-the-art in small-scale solar-powered UAV *perpetual flight* performance.

---

<sup>7</sup>Note that estimating  $T_{\text{cm}}$  is generally harder than estimating  $T_{\text{exc}}$  because  $T_{\text{cm}}$  depends on both the very uncertain  $P_{\text{solar}}$  and  $P_{\text{out}}$  over the day, while  $T_{\text{exc}}$  only depends on the better-known  $P_{\text{out}}$  at night.

## 5.1 Varying Operating Date and Location

Figure 17 answers the question when and where *perpetual flight* is possible<sup>8</sup>. The results are shown for the northern hemisphere and use the axis-symmetry with respect to the northern solstice on June 21<sup>st</sup>. At its design point of  $\varphi_{\text{lat}} = 47^\circ\text{N}$ , *AtlantikSolar* provides a  $\pm 3$ -month *perpetual flight* window around June 21<sup>st</sup>. This clearly verifies and even exceeds the central requirement defined during *AtlantikSolar*'s conceptual design process in section 2.3. Year-round *perpetual flight* is possible at the equator and up to  $\varphi_{\text{lat}} = 27^\circ\text{N}$ . In summer, the excess time increases with higher latitudes due to the increased daylight duration. For  $\varphi_{\text{lat}} > 80^\circ\text{N}$ , the excess time is undetermined because we always have  $P_{\text{solar}} > P_{\text{out}}$  and the battery is thus never discharged. In theory, in many parts of the Arctic and Antarctic the aircraft could thus be flown perpetually without batteries. Overall, the distribution between  $T_{\text{exc}}$  and  $T_{\text{cm}}$  is well balanced. This underlines that for all latitudes and days of the year, the design process has led to well-balanced robustness against both power income reductions (e.g. clouds) and power consumption increases (e.g. turbulence and downdrafts). When *perpetual flight* is not possible, the flight endurance is still up to  $T_{\text{endur}} = 48\text{ h}$ <sup>9</sup>.

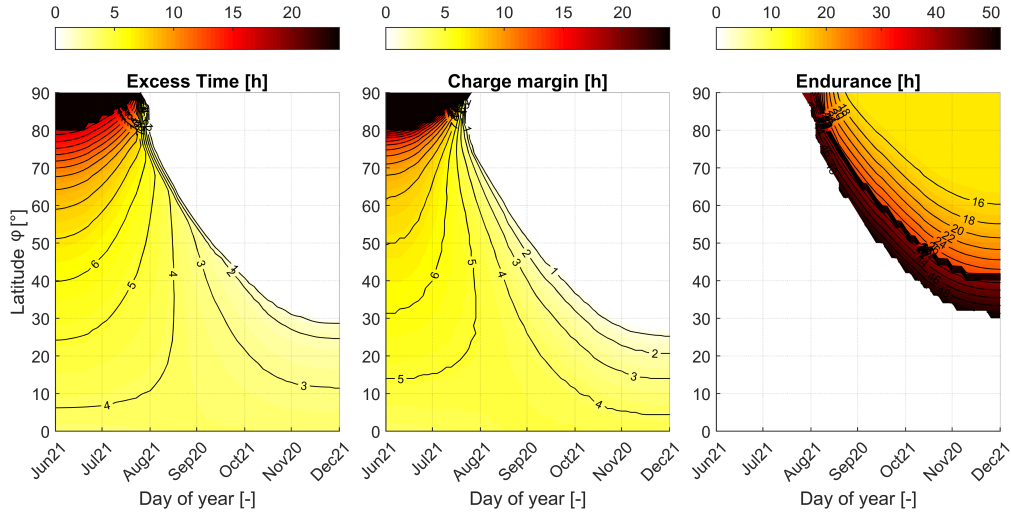


Figure 17: Estimated excess time  $T_{\text{exc}}$ , charge margin  $T_{\text{cm}}$  and endurance  $T_{\text{endur}}$  for the final *AtlantikSolar* UAV configuration versus a range of latitudes and times of the year. Note that the endurance contours fill exactly the area where  $T_{\text{exc}} \leq 0$  and where *perpetual flight* is thus not feasible.

## 5.2 Varying Meteorological Conditions

Figure 18 focuses on *perpetual flight* robustness against deteriorated meteorological conditions. The disturbances are represented by the ratios of  $P_{\text{solar}}$  and  $P_{\text{out}}$  to their nominal values  $P_{\text{solar}}^{\text{nom}}$  and  $P_{\text{out}}^{\text{nom}}$  that are as before defined by the cloud cover factor and the output power factor of section 2.4. The results are given for June 21<sup>st</sup> at the design latitude  $\varphi_{\text{lat}} = 47^\circ\text{N}$ . At nominal power consumption, *perpetual flight* is possible down to 40 % of  $P_{\text{solar}}^{\text{nom}}$ , and at nominal power income, *perpetual flight* is possible at up to 50 % increased power consumption. The result from the conceptual design phase (Figure 5) is thus largely confirmed. The achieved energetic margins are significant with respect to previous solar-powered UAV designs such as SkySailor (Noth, 2008a). Note that the probability of long-term power consumption increases of the aforementioned magnitude is low because it is mostly caused by local thermal downdrafts that can be avoided by appropriate downdraft-avoidance algorithms. However, significant cloud cover cannot be avoided, and

<sup>8</sup>For the following sections, we assume  $\sigma_{\text{bat}} = 10\%$  ( $T_{\text{exc}} \approx 1.5\text{ h}$ ) a reasonable bound to declare *perpetual flight* as feasible. Below that, the energetic margins are too low to guarantee safe flight in significant turbulence or in a go-around during a landing. In addition, we assume launch of the aircraft at  $t_{\text{sr}}$  with  $\sigma_{\text{bat}} = 90\%$ . For  $T_{\text{cm}}$  and  $T_{\text{exc}}$ , we give a *steady-state* value that we approximate by giving the second-day instead of first-day performance metrics (see Figure 3).

<sup>9</sup>The discontinuity in the endurance plot separates the case where the aircraft is able to cross the first night (but does not fully recharge during the second day and thus cannot cross the next night), or does not even manage to cross the first night.

given that clouds can quickly lead to considerable power income reductions (Matuszko, 2012) the estimated margins can only be considered a first step towards meteorologically-robust solar-powered *perpetual flight*.

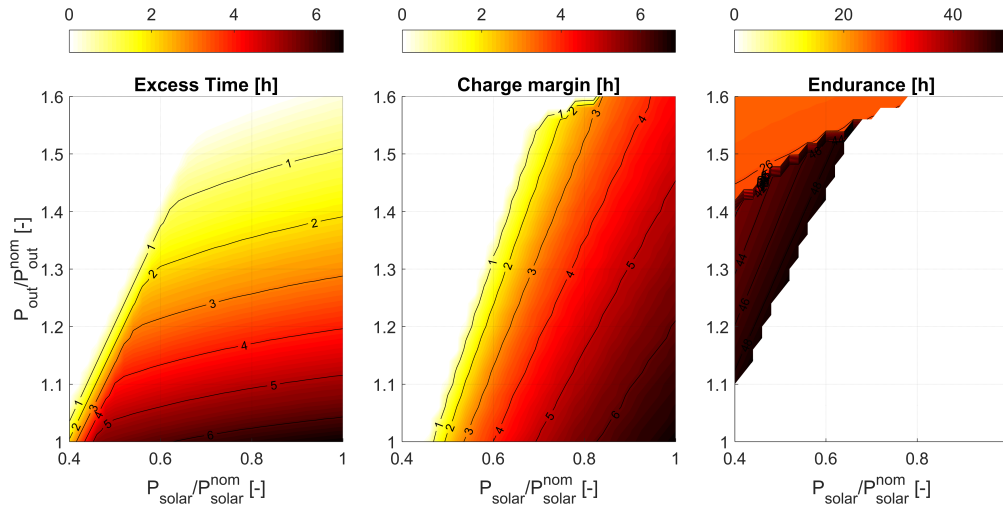


Figure 18: Estimated excess time  $T_{\text{exc}}$ , charge margin  $T_{\text{cm}}$  and endurance  $T_{\text{endur}}$  for the final *AtlantikSolar* UAV configuration versus increased power consumption  $P_{\text{out}}$  and decreased power income  $P_{\text{solar}}$ . Note that the endurance contours fill exactly the area where  $T_{\text{exc}} \leq 0$  and thus *perpetual flight* is not feasible.

### 5.3 Applications With Payload

No solar-powered low-altitude robotic aircraft has ever been used in a real-world *perpetual flight* application before. *AtlantikSolar* has been used in search-and-rescue applications (Oettershagen, Stastny, et al., 2015), but not in a *perpetual flight* setting. However, the increased energetic margins of *AtlantikSolar* clearly allow first *perpetual flight* aerial sensing- and mapping-applications. Figure 19 shows the estimated performance over a set of payload configurations for  $\varphi_{\text{lat}} = 47^\circ\text{N}$  versus the day-of-year  $\delta$ . When considering the aforementioned  $\sigma_{\text{bat}} = 10\%$  as a limit for *perpetual flight* feasibility, the no-payload configuration nearly yields a  $\pm 3.5$ -month perpetual endurance window around June 21<sup>st</sup>. A small optical camera payload ( $m_{\text{pld}} = 0.2\text{ kg}$ ,  $P_{\text{pld}} = 2.5\text{ W}$ ) reduces that window to 3 months, and a heavier and more power-hungry infrared-camera combined with a data-downlink or low-power onboard computer ( $m_{\text{pld}} = 0.4\text{ kg}$ ,  $P_{\text{pld}} = 5\text{ W}$ ) reduces it to around 2 months. The absolute *perpetual flight* payload limit for the specific *AtlantikSolar* UAV configuration with  $m_{\text{bat}} = 2.92\text{ kg}$  lies at  $m_{\text{pld}} = 0.8\text{ kg}$  and  $P_{\text{pld}} = 10\text{ W}$ , which already allows the integration of better on-board computers, but only barely allows *perpetual flight* operation in mid-June. The flight endurance is however still significant with this payload size (Oettershagen, Stastny, et al., 2015).

Overall, solar-powered UAVs such as *AtlantikSolar* can already carry the mass of camera-and-compute payloads (e.g. the sensor pod of section 3.1.5 with  $m_{\text{pld}} = 480\text{ g}$ ) needed for both application-related sensing as well as on-board autonomy (map generation, obstacle avoidance and path planning) during *perpetual flight* missions. However, the power requirements for the full on-board autonomy are usually too high despite the use of power-efficient on-board computers ( $P_{\text{pld}}^{\text{max}} = 15\text{ W}$  for ETH Zurich’s sensor pod). Figure 19 however also reveals that the payload decreases  $T_{\text{cm}}$  much less than  $T_{\text{exc}}$  because the payload power is small compared to the significant incoming solar power. A correct battery sizing to the specific payload — e.g. through the conceptual design framework of this paper — is thus a necessity to allow solar-powered *perpetual flight* with large payloads. For example, the increase from  $m_{\text{bat}} = 2.92\text{ kg}$  to  $m_{\text{bat}} = 3.8\text{ kg}$  in Figure 19 balances  $T_{\text{exc}}$  and  $T_{\text{cm}}$  again, doubles  $T_{\text{exc}}$  and brings the *perpetual flight* window back to  $\pm 2$  months.

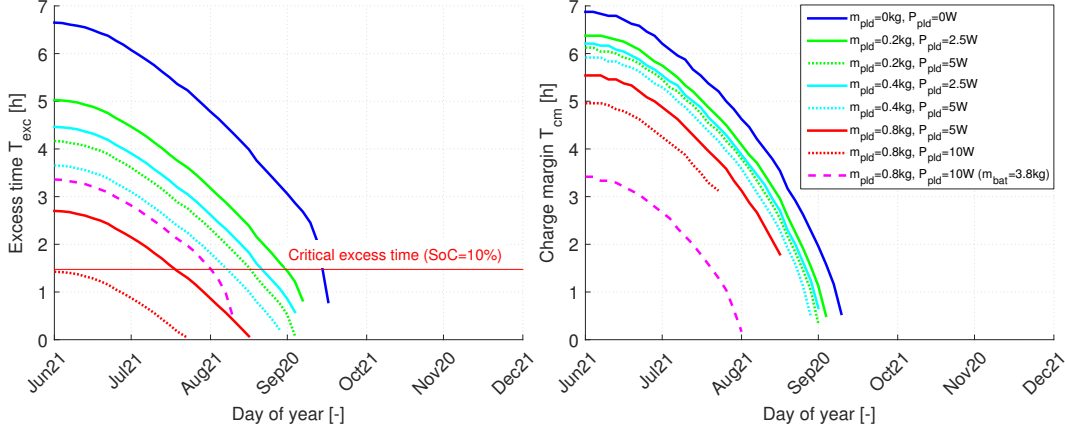


Figure 19: Estimated excess time  $T_{\text{exc}}$  and charge margin  $T_{\text{cm}}$  for the *AtlantikSolar* UAV with different payloads against the day-of-year at  $\varphi_{\text{lat}} = 47^\circ\text{N}$ .

#### 5.4 Performance Perspectives and Sensitivity Analysis

The energetic margin improvements provided by *AtlantikSolar* over previous solar-powered UAV designs are significant, but as section 5.2 explains, they are still only an initial step towards actual energetically-robust solar-powered *perpetual flight* in the lower atmosphere. Therefore, it is important to analyze where potential improvements are most likely to come from. Candidates are the

- *Low-level flight controller tracking performance.* The expected improvements are small, because as shown in section 3.2.3, even simple PID-based flight control structures can achieve good stabilization close to the optimal aircraft operating point.
- *High-level aircraft intelligence.* This includes large-scale energy-optimal meteorology-aware (clouds, winds, precipitation) path planning (Rubio & Kragelund, 2003; Wirth, Oettershagen, Ambuehl, & Siegwart, 2015), more local planning in dynamic wind fields (Chakrabarty & Langelaan, 2013), and tracking of single thermal updrafts through in-situ climb rate measurements (Edwards & Silverberg, 2010). These approaches promise significant improvements in *perpetual flight* performance, but require certain degrees of freedom in the mission trajectory. Their applicability e.g. to a fixed-position aerial observation mission thus needs to be assessed case-by-case.
- *Sensing capability per payload mass and power requirement.* The on-going miniaturization of sensors is a central element increasing the operational value of solar-powered UAVs. The effects of payload miniaturization on the *perpetual flight* performance are indicated in Figure 19.
- *Aircraft technological parameters.*

The aircraft technological parameters are the most probable source of improvement because they affect the *perpetual flight* performance independent of the operating conditions, mission type or payload. Figure 20 therefore investigates the sensitivity of  $T_{\text{exc}}$  and  $T_{\text{cm}}$  on a relative change (to the current *AtlantikSolar* configuration) of the following technological parameters:

- A *battery specific energy density*  $e_{\text{bat}}$  change of +10% ( $251 \text{ Wh/kg} \rightarrow 276.1 \text{ Wh/kg}$ ) increases the total battery-powered flight time proportionally and thus  $T_{\text{exc}}$  by +26%. Due to the increased  $E_{\text{bat}}$ ,  $T_{\text{cm}}$  is slightly decreased. These improvements seem feasible given the historical growth in Li-Ion specific energy density of  $5.5 \text{ Wh/kg}$  per year reported by Zu and Li (2011) for 1990–2010. The same authors mention Lithium-Sulfur (Li-S) batteries, a technology which was already used with  $e_{\text{bat}} = 350 \text{ Wh/kg}$  on the Zephyr solar-powered HALE UAV (Sion Power, 2014).
- A *solar module efficiency*  $\eta_{\text{sm}}$  change of +10% ( $23.7\% \rightarrow 26.1\%$ ) improves  $T_{\text{exc}}$  by 1% and

$T_{\text{cm}}$  by +5.3%. Ways to achieve 26% cell efficiency for the mono-Si cells used on *AtlantikSolar* have been identified (Smith et al., 2014). However, these efficiencies have not been achieved in laboratories yet (National Renewable Energy Laboratory, 2016) and thus commercial availability lies years ahead. Thin gallium arsenide (GaAs) cells with up to  $\eta_{\text{sm}} = 30\%$  have however already been demonstrated on UAVs (The Economist, 2013). They also offer lower mass per area and greater structural flexibility than mono-Si cells at an order-of-magnitude price premium.

- A *propulsion efficiency*  $\eta_{\text{prop}}$  change has the largest positive effect: A +10% change (62%  $\rightarrow$  68.2%) results in  $P_{\text{prop}}^{\text{level}}$ : 36 W  $\rightarrow$  32.73 W, thereby decreases  $P_{\text{out}}$  during both day and night, and thus increases  $T_{\text{exc}}$  by +23% and  $T_{\text{cm}}$  by +5.5%. The large sensitivity of the performance metrics on  $\eta_{\text{prop}}$  is the very reason why *AtlantikSolar*'s propulsion system has been optimized that extensively (see section 3.3.3). As a consequence, further improvements in  $\eta_{\text{prop}}$  can only be achieved with significant effort. Larger UAVs would however automatically benefit from scaling effects that increase their propulsion system efficiency (Noth, 2008a).
- *Aircraft dry mass*  $m_{\text{dry}}$  reductions have a similarly significant effect: A -10% change ( $m_{\text{dry}}$ : 4.0 kg  $\rightarrow$  3.6 kg) causes a 22% increase in  $T_{\text{exc}}$  and a 4% increase in  $T_{\text{cm}}$  because of the resulting  $P_{\text{out}}$  decrease. However, of the masses in Table 4,  $m_{\text{struct}}$  and  $m_{\text{prop}}$  are already extremely optimized,  $m_{\text{av}}$  could only be reduced by 10–15% with significant effort, and  $m_{\text{sm}}$  could be optimized by up to 40% only by switching to the much more expensive GaAs technology. A  $m_{\text{dry}}$  decrease of 0.52 kg (13%) is thus attainable, but only at a significant cost surcharge.

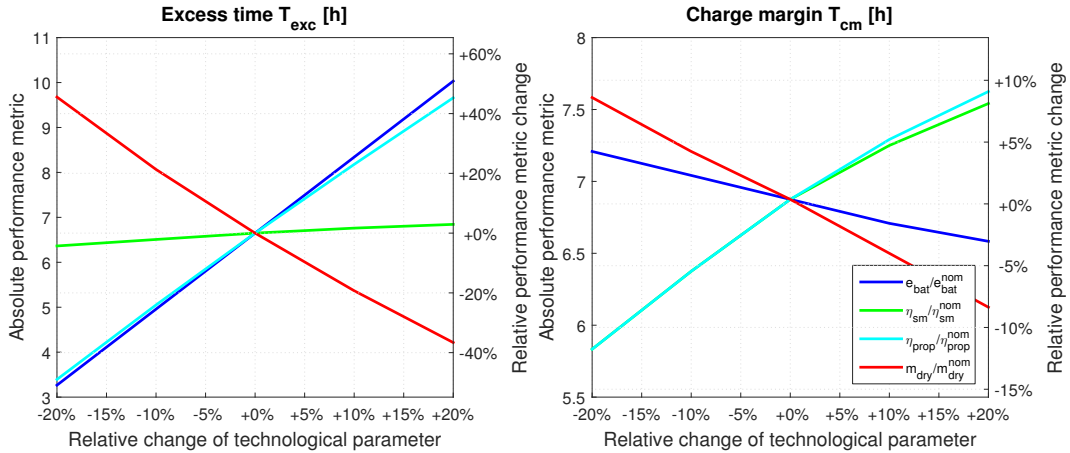


Figure 20: Absolute- and relative change of  $T_{\text{exc}}$  and  $T_{\text{cm}}$  per change in the aircraft technological parameters.

Overall, the main headroom in solar UAV *perpetual flight* performance lies in battery technology and, to a lesser extent, in decreased solar module weight and increased efficiency. Especially the current focus on battery technology for electric vehicles and mobile devices leads to incremental improvements through which solar-powered UAVs will automatically benefit. The wide commercial availability of high energy density battery technology such as Li-S would clearly represent a breakthrough for the performance and operational value of solar-powered UAVs in *perpetual flight* applications.

## 6 Lessons Learned

Developing robotic aerial vehicles is neither a risk-free nor a straightforward process. This section summarizes the main *lessons learned* during the three-year *AtlantikSolar* design process to help other solar-powered UAV designers avoid common mistakes. Apart from the significant amount of experience and the iterative design approach required during all development phases, the main lessons learned are:

## Technology:

- *Solar power income prediction:* For accurate UAV performance prediction and design, Eq. (11) should be augmented with an angle-of-incidence dependent  $\eta_{sm}$  as early as possible (section 3.3.1).
- *Mass prediction:* The conceptual design stage’s accuracy in predicting the solar-powered UAV’s mass is greatly enhanced by using small-scale structure- or solar-module samples (section 3.3.2).
- *Power consumption:* Achieving a  $P_{out}$  that allows solar-powered *perpetual flight* is very challenging, as it requires (a) efficient aerodynamics (b) efficient propulsion and (c) a well-functioning autopilot. Initial manually-piloted flights showed that  $P_{out} \approx 70$  W, which does not allow perpetual flight. Using and optimizing the flight controller yielded  $P_{out} \approx 55$  W. Significant propulsion system optimizations (section 3.3.3) were required to yield the final  $P_{out}^{AS-2} \approx 42$  W.

## Flight operations:

- *Multi-stage flight testing process:* The used and recommended test process for each change to safety-critical avionics is (a) unit-level bench test (b) system-level bench test (c) flight test on small test platforms (d) flight test on the full-scale solar-powered UAV. Especially the tests on smaller platforms with the same avionics (Oettershagen et al., 2014) have uncovered flaws and avoided unsafe situations on *AtlantikSolar*.
- *Emergency situations:* In-flight emergency situations included
  - A seemingly spontaneous flight controller crash after four hours of autopilot-controlled flight. This underlines the need for (a) thorough long-term autopilot testing and (b) a manual RC-override functionality, which in our case helped to save the airplane.
  - Three propulsion system failures caused by malfunctioning gearboxes after 3, 6 and 28 hours of flight. The safety pilot landed the plane without propulsion power. After the incidents, the gearbox was changed to a heavier all-steel gearbox which has lasted 15 days under nominal loads in lab-tests and was also used for the 81-hour flight. In contrast, the control surface servomotors never failed. This may be a result of the extensive 30-day long-term test performed (section 3.1.3).
- *Crashes:* During the extensive flight campaigns, the *AtlantikSolar* UAVs faced three crashes (but could be repaired). The reasons for the two crashes for which flight logs could be recovered were
  - A complete RC transmitter failure. The crash happened at the beginning of the project when no autopilot was installed yet. The current autopilot would have initiated an autonomous loitering maneuver.
  - A structural failure. While manually-controlled in windy conditions, the aircraft entered a dive, and when re-activated, the autopilot attempted to correct using full elevator. The dynamic overload protection of section 3.2.3 was consequently added.

In general, successful solar-powered UAV flight testing requires a very systematic and procedure-based (e.g. check lists) approach to flight operations and a proactive approach towards detecting and correcting anomalies. The persistent implementation of these elements was decisive for the achievements of *AtlantikSolar*.

## 7 Conclusion

This paper has presented the development efforts behind the solar-powered hand-launchable *AtlantikSolar*, a UAV that recently demonstrated an 81-hour *perpetual flight* that is currently the longest continuous flight of any aircraft below 50 kg mass. The paper brings together aircraft design and robotic technologies to establish the current state-of-the-art in robotic solar-powered *perpetual flight* performance of small UAVs.

More specifically, we have introduced and released (Oettershagen, 2016b) a conceptual design and analysis framework to simulate, design and analyze solar-powered UAVs and their precise energetic performance. The framework is applied to design the 5.6 m and 6.93 kg *AtlantikSolar* UAV. The vehicle is based on the most energy-dense battery technology publicly available today, uses efficient yet affordable solar modules and implements a custom-designed state estimation- and flight control framework that is optimized for solar-powered UAVs but operates on top of an off-the-shelf Pixhawk autopilot. Flight results from *AtlantikSolar*'s 81-hour continuous *world endurance record* flight released at (Oettershagen, 2016a) are analyzed to retrieve the achieved performance metrics and to verify the design approach. Two main conclusions can be drawn:

- *Conceptual design and analysis methodology verified:* Via the 81-hour and 28-hour flight data, we provide the first in-depth error-analysis of a conceptual design and analysis framework for solar-powered *perpetual flight*-capable UAVs in the literature. When the identified crucial physical effects affecting the energy balance (e.g. the angle-of-incidence dependence of the solar module efficiency) are considered, our design framework can be used to design solar-powered UAVs to a performance metric accuracy of below 7.5 %.
- *Significant improvement of perpetual flight performance achieved:* AtlantikSolar's 81-hour and a previous 28-hour flight show that a minimum state-of-charge of  $\sigma_{\text{bat}}^{\text{min}} = 39\%$  ( $T_{\text{exc}} = 6.8$  h) and a charge margin of  $T_{\text{cm}} = 6.2$  h are achievable in summer at mid-European latitudes. These performance metrics are a clear improvement over previous record-breaking solar-powered LALE UAVs such as SkySailor (Noth, 2008a) with  $T_{\text{cm}} < 3$  h and  $\sigma_{\text{bat}}^{\text{min}} = 5.8\%$ , and SoLong (Cocconi, 2005), which had to employ thermal updraft tracking (Noth, 2008b). Due to the novel conceptual design approach presented in this paper, these performance margins are not only larger than for previous UAVs, but are also well-balanced and thus provide higher robustness against deteriorated weather or changed operating conditions. As a result, both year-round robotic *perpetual flight* at and around the equator as well as robotic *perpetual flight* missions with small optical- or infrared-camera systems become feasible on small-scale solar-powered UAVs for the first time.

Overall, this paper has laid initial groundwork for future *perpetual flight* applications with payload-equipped solar-powered UAVs in real missions ranging from the equator over medium latitudes to the Arctic and Antarctic. The respective design methodologies and knowledge are in place. While research questions in optimal control and -navigation remain, the future progress in the *perpetual flight* performance of solar-powered UAVs now mainly depends on the progress in energy generation and especially -storage technology.

## Acknowledgments

This work was supported by the EU-FP7 research projects ICARUS and SHERPA as well as a number of project partners and generous individuals. We'd like to thank Rainer Lotz and Adrian Eggenberger for acting as safety pilots, Rainer Lotz for manufacturing the airplane structure, Dieter Siebenmann for the structural dimensioning, and all project partners<sup>10</sup> for their significant contributions to the project.

## References

- Ackerman, E. (2013). Giant Solar-Powered UAVs are Atmospheric Satellites. IEEE Spectrum. Retrieved from <http://spectrum.ieee.org/automaton/robotics/aerial-robots/giant-solar-powered-uavs-are-atmospheric-satellites>
- AeroVironment. (2013). AeroVironment Solar-Powered Puma AE Small Unmanned Aircraft Achieves Continuous Flight for More Than Nine Hours. Press Release. Retrieved from [http://www.avinc.com/resources/press\\_release/aerovironment-solar-powered-puma-ae-small-unmanned-aircraft-achieves-contin](http://www.avinc.com/resources/press_release/aerovironment-solar-powered-puma-ae-small-unmanned-aircraft-achieves-contin)

---

<sup>10</sup>A list of project partners is available at [http://www.atlantiksolar.ethz.ch/?page\\_id=187](http://www.atlantiksolar.ethz.ch/?page_id=187)

- Boucher, R. J. (1984). History of Solar Flight. In *AIAA/SAE/ASME 20<sup>th</sup> Joint Propulsion Conference*.
- ByeAerospace. (2015). Industry First: Solar-Electric Silent Falcon Prepares for Initial Customer Orders. Press Release. Retrieved from <http://www.byeaerospace.com/press/industry-first-solar-electric-silent-falcon%E2%84%A2-prepares-for-initial-customer-orders.aspx>
- Chakrabarty, A. & Langelaan, J. (2013). UAV Flight Path Planning in Time Varying Complex Wind-Fields. In *American Control Conference (ACC)*.
- Cocconi, A. (2005). *AC Propulsion's solar electric powered SoLong UAV*. AC Propulsion. Retrieved from <https://archive.org/details/ACPropulsionSolongUAV2005>
- Colella, N. & Wenneker, G. (1996). Pathfinder: Developing a solar rechargeable aircraft. *IEEE Potentials*, 15(1), 18–23.
- DellaCa, L. (2013). *Load Modeling and Reliability Analysis for Actuators on solar powered UAVs* (Bachelor thesis, ETH Zurich).
- Dorobantu, A., Murch, A., Mettler, B., & Balas, G. (2011). Frequency domain system identification for a small, low-cost, fixed-wing UAV. In *Proceedings of the 2011 AIAA Guidance, Navigation, and Control Conference*.
- Drela, M. (2001). *XFOIL 6.9 User Primer*. MIT Aero&Astro. Retrieved from <http://web.mit.edu/drela/Public/web/xfoil/xfoil-doc.txt>
- Duffie, J. A. & Beckman, W. A. (2006). *Solar Engineering of Thermal Processes* (3<sup>rd</sup> ed.). Wiley.
- Edwards, D. J. & Silverberg, L. M. (2010). Autonomous Soaring: The Montague Cross-Country Challenge. *Journal of Aircraft*, 47.
- Leutenegger, S. (2014). *Unmanned Solar Airplanes: Design and Algorithms for Efficient and Robust Autonomous Operation* (Doctoral dissertation, ETH Zurich).
- Leutenegger, S., Jabas, M., & Siegwart, R. (2010). Solar airplane conceptual design and performance estimation. *Journal of Intelligent Robot Systems*, 61, 545–561.
- Leutenegger, S., Melzer, A., Alexis, K., & Siegwart, R. (2014). Robust State Estimation for Small Unmanned Airplanes. In *IEEE Multi-conference on Systems and Control*.
- Malaver, A. J. R., Gonzalez, L. F., Motta, N., & Villa, T. F. (2015). Design and Flight Testing of an Integrated Solar Powered UAV and WSN for Remote Gas Sensing. In *IEEE Aerospace Conference*.
- Matuszko, D. (2012). Influence of the extent and genera of cloud cover on solar radiation intensity. *International Journal of Climatology*, 32(15), 2403–2414. DOI: 10.1002/joc.2432.
- Meier, L., Honegger, D., & Pollefeys, M. (2015). PX4: A Node-Based Multithreaded Open Source Robotics Framework for Deeply Embedded Platforms. In *IEEE International Conference on Robotics and Automation (ICRA)*.
- Morton, S., D'Sa, R., & Papanikolopoulos, N. (2015). Solar Powered UAV: Design and Experiments. In *IEEE International Conference on Intelligent Robots and Systems (IROS)*.
- Morton, S., Scharber, L., & Papanikolopoulos, N. (2013). Solar Powered Unmanned Aerial Vehicle for Continuous Flight: Conceptual Overview and Optimization. In *IEEE International Conference on Robotics and Automation (ICRA)*.
- Mosimann, L. (2014). *Robust Fixed Wing Control against Actuator Faults* (Master's thesis, ETH Zurich).
- National Renewable Energy Laboratory. (2016). Best Research-Cell Efficiencies. Accessed: 2016-03-25. Retrieved from <http://www.nrel.gov/ncpv/>
- Nikolic, J., Rehder, J., Burri, M., Gohl, P., Leutenegger, S., Furgale, P. T., & Siegwart, R. Y. (2014). A Synchronized Visual-Inertial Sensor System with FPGA Pre-Processing for Accurate Real-Time SLAM. In *IEEE International Conference on Robotics and Automation (ICRA)*.
- Noth, A. (2008a). *Design of Solar Powered Airplanes for Continuous Flight* (Doctoral dissertation, ETH Zurich).
- Noth, A. (2008b). History of Solar Flight. Autonomous Systems Lab, ETH Zurich. Retrieved from <http://www.sky-sailor.ethz.ch/docs/History%20of%20Solar%20Flight%20v2.0-%20A.Noth%202008.pdf>
- Oettershagen, P. (2016a). AtlantikSolar 81-hour Perpetual Flight. Dataset Release. Retrieved from <http://projects.asl.ethz.ch/datasets/doku.php?id=JFR2016>
- Oettershagen, P. (2016b). Conceptual Design and Analysis Framework for Solar-powered UAVs. Software Release. Retrieved from [https://github.com/ethz-asl/fw\\_conceptual\\_design](https://github.com/ethz-asl/fw_conceptual_design)
- Oettershagen, P. (2017). *High-Fidelity Solar Power Income Modeling for Solar-Electric UAVs: Development and Flight Test Based Verification*. ETH Zurich. arXiv: 1703.07385 [cs.R0]

- Oettershagen, P., Melzer, A., Leutenegger, S., Alexis, K., & Siegwart, R. (2014). Explicit Model Predictive Control and  $\mathcal{L}_1$ -Navigation Strategies for Fixed-Wing UAV Path Tracking. In *22nd Mediterranean Conference on Control & Automation (MED)*.
- Oettershagen, P., Melzer, A., Mantel, T., Rudin, K., Lotz, R., Siebenmann, D., ... Siegwart, R. (2015). A Solar-Powered Hand-Launchable UAV for Low-Altitude Multi-Day Continuous Flight. In *IEEE International Conference on Robotics and Automation (ICRA)*.
- Oettershagen, P., Melzer, A., Mantel, T., Rudin, K., Stastny, T., Wawrzacz, B., ... Siegwart, R. (2016). Perpetual flight with a small solar-powered UAV: Flight results, performance analysis and model validation. In *IEEE Aerospace Conference*.
- Oettershagen, P., Stastny, T., Mantel, T., Melzer, A., Rudin, K., Gohl, P., ... Siegwart, R. (2015). Long-Endurance Sensing and Mapping using a Hand-Launchable Solar-Powered UAV. In *Field and Service Robotics (FSR)*.
- Osborne, T. (2016). U.K. Will Buy Two Zephyr 8 UAVs. Aviationweek Aerospace Daily. Retrieved from <http://aviationweek.com/awindefense/uk-will-buy-two-zephyr-8-uavs>
- Panasonic. (2014). Lithium Ion Handbook. Retrieved from [http://eu.industrial.panasonic.com/sites/default/pidseu/files/downloads/files/li-ion\\_handbook\\_22\\_10\\_15.pdf](http://eu.industrial.panasonic.com/sites/default/pidseu/files/downloads/files/li-ion_handbook_22_10_15.pdf)
- Park, S., Deyst, J., & How, J. P. (2004). A new nonlinear guidance logic for trajectory tracking. In *AIAA Guidance, Navigation, and Control Conference and Exhibit* (pp. 16–19).
- QinetiQ. (2010). QinetiQ files for three world records for its Zephyr Solar powered UAV. Press Release. Retrieved from <http://www.qinetiq.com/media/news/releases/Pages/three-world-records.aspx>
- Rubio, J. C. & Kragelund, S. (2003). The Trans-Pacific Crossing: Long Range Adaptive Path Planning for UAVs through Variable Wind Fields. In *IEEE Digital Avionics Systems Conference*.
- S. Park, J. Deyst and J. P. How. (2007). Performance and Lyapunov stability of a nonlinear path following guidance method. *Journal of Guidance, Control, and Dynamics*, 30(6), 1718–1728.
- Sion Power. (2014). Sion Power's Lithium-Sulfur Batteries Power High Altitude Pseudo-Satellite Flight. Press Release. Retrieved from <http://sionpower.com/media-center.php?code=sion-powers-lithiumsulfur-batteries-power-high-alt>
- Smith, D. D., Cousins, P., Westerberg, S., De Jesus-Tabajonda, R., Aniero, G., & Shen, Y.-C. (2014). Toward the Practical Limits of Silicon Solar Cells. *IEEE Journal of Photovoltaics*, 4, 1465.
- Stull, R. B. (1988). *An Introduction to Boundary Layer Meteorology* (1<sup>st</sup> edition). Springer.
- The Economist. (2013). On a bright new wing: Small, remote-controlled craft powered by the sun are taking to the air. Accessed: 2016-03-25. Retrieved from <http://www.economist.com/news/science-and-technology/21584962-small-remote-controlled-craft-powered-sun-are-taking-air>
- Tischler, M. B. & Remple, R. K. (2012). *Aircraft and Rotorcraft System Identification: Engineering Methods with Flight Test Examples*. American Institute of Aeronautics and Astronautics (AIAA).
- Vempati, A., Agamennoni, G., Stastny, T., & Siegwart, R. (2015). Victim Detection from a Fixed-wing UAV: Experimental Results. In *International Symposium on Visual Computing (ISVC)*.
- Weider, A., Levy, H., Regev, I., Ankri, L., Goldenberg, T., Ehrlich, Y., ... Cohen, M. (2007). *SunSailor: Solar powered UAV*. Aerospace Engineering Faculty, Technion. Retrieved from <http://webee.technion.ac.il/people/maxcohen/SunSailorArt19nov06.pdf>
- Wirth, L., Oettershagen, P., Ambuehl, J., & Siegwart, R. (2015). Meteorological Path Planning Using Dynamic Programming for a Solar-Powered UAV. In *IEEE Aerospace Conference*.
- Zu, C.-X. & Li, H. (2011). Thermodynamic analysis on energy densities of batteries. *Energy & Environmental Science*, 4(8), 2614. DOI: 10.1039/c0ee00777c.